Transverse Single-Spin Asymmetry for Diffractive Electromagnetic Jets with $p^{\uparrow} + p$ Collisions at $\sqrt{s} = 200$ GeV

Xilin Liang

March 21, 2025

Contents

List of Figures

List of Tables

Chapter 1

Introduction

Transverse single-spin asymmetries (A_N), which are defined as left-right asymmetries of the particle production with respect to the plane defined by the momentum and spin directions of the polarized beam, have been observed to be large for charged- and neutral-hadron production in hadron-hadron collisions over a couple of decades [1, 2, 3, 4, 5]. In pQCD, however, the A_N is predicted to be small and close to zero in high energy collisions [6]. There are two major frameworks that can provide a potential explanation for such sizeable asymmetries. The first one is the transverse-momentum-dependent (TMD) contributions from the initial-state quark and gluon Sivers functions and/or the final-state Collins fragmentation functions. In the Sivers mechanism, the asymmetry comes from the correlation between the proton spin and the parton transverse momentum [7], while the Collins effect arises from the correlation between the spin of the fragmenting quark and the outgoing hadron's transverse momentum [8]. Another framework is based on the twist-3 contributions in the collinear factorization framework, including the quark-gluon or gluon-gluon correlations and fragmentation functions [9].

According to the study by CMS Collaboration [10], diffractive interactions contribute to about a significant fraction ($\sim$ 25%) of the total inelastic p+p cross section at high energies. The simulation for hard diffractive events based on PYTHIA-8 predicts that the fraction of diffractive cross section in the total inclusive cross section at the forward region is about 20% [4]. In recent years, analyses of A_N for forward π^0 and electromagnetic jets (EM-jets) in $p^{\uparrow} + p$ collisions at STAR indicated that there might be non-trivial contributions to the large A_N from diffractive processes [5, 11]. Measuring the A_N of diffractive process will provide an opportunity to study the properties and understand the diffractive exchange in p+p collisions.

In this study, we will explore the A_N for the events with unpolarized proton intact (single diffractive process) and the events with polarized proton intact (the semi-exclusive process).

Chapter 2

Dataset and Quality Assurance (QA)

2.1 General information for the dataset

The single diffractive and the semi-exclusive EM-jet A_N analyses utilize polarized p+p collision at $\sqrt{s} = 200$ GeV taken in run 15. Details of the data set are listed as follow:

- Trigger setup name: production_pp200trans_2015
- Data stream: fms
- Production tag: P15ik
- File type: MuDst files in Distributed Disk (DD)

The analysis generates smaller size data stream files (NanoDst) from the MuDst files, applying trigger filter (described in Sec. (2.2)) and jet reconstruction (described in Sec. 3.1). In addition, the events with at least one Roman Pot track are required for diffractive EM-jet A_N analysis when generating the DST files.

2.2 Triggers

9 triggers for FMS are used for this analysis. The triggers with their ID are listed in Table (2.1). However, the FMS-sm-bs3 trigger is also considered a source of background. Therefore, the effect of this trigger will be studied as systematic uncertainty, which will be explained in 8.3.

Table 2.1: Trigger name lists and trigger ID for run 15

Trigger name	Trigger ID
FMS-JP0	480810 / 480830
FMS-JP1	480809 / 480829
FMS-JP2	480808 / 480828
FMS-sm-bs1	480801 / 480821 / 480841
FMS-sm-bs2	480802 / 480822
FMS-sm-bs3	480803 / 480823 / 480843
FMS-lg-bs1	480804 / 480824 / 480844
FMS-lg-bs2	480805 / 480825
FMS-lg-bs3	480806 / 480826

2.3 Calibration

The calibration for run 15 FMS dataset are from existing STAR framework [12], but with some additional steps. They mainly include the following items:

- Bit shift (BS): It refers to the binary bit, used to store the ADC value, not starting from the normal lowest bit. The BS will affect a cell's ADC distribution and the corresponding hit energy. The approach to check the BS is to use the ADC of each FMS hit to check with its corresponding BS value of the cell [12].

- Gain and gain correction: The energy of the hit = ADC × gain × gain correction. The gain is the calculated value based on a cell's η position, while the gain correction is obtained from offline calibration [12]. The flag of the gain and the gain correction for each tower in the STAR database is "fmsGainCorr-BNL-C".

- Hot channel and bad channel masking: A hot channel refers to the tower with a number of hits far more than the average number of hits for the whole detector towers within some time range. A bad channel refers to the problematic towers that might suffer from hardware issues. Both hot and bad channels can affect the quality of the calibration and the analyses since there are quite a lot of non-physical signals that are contaminated. To mask out these channels, the gain values are set to zero. In addition to

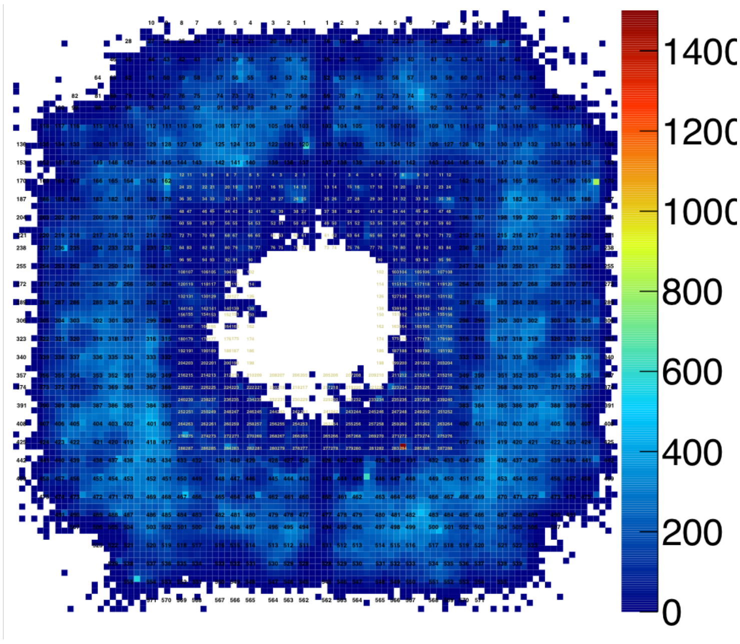

Figure 2.1: Example of EM-jet distribution at FMS before additional hot channel masking. The red color area in this plot indicates the possible hot channels.

the existing hot channel and bad channel masking from STAR calibration [12], the fill-by-fill hot channel masking is applied in this analysis. The EM-jet distribution before any event selections for every fill is checked to find out any possible hot channels. The EM-jet reconstruction is discussed in 3.1. Figure (2.1) shows one example of the EM-jet distribution at the FMS. The areas with extremely high EM-jet entries compared to the overall average entries in the plot are assumed to be the hot channel area. The channels within these areas are considered hot channels and added manually to the hot channel lists. Figure (2.2) shows the EM-jet distribution for fill 18827 as an example after the additional hot channel masking. From the plot, the hot channels disappear, and the majority of towers have entries close to the average.

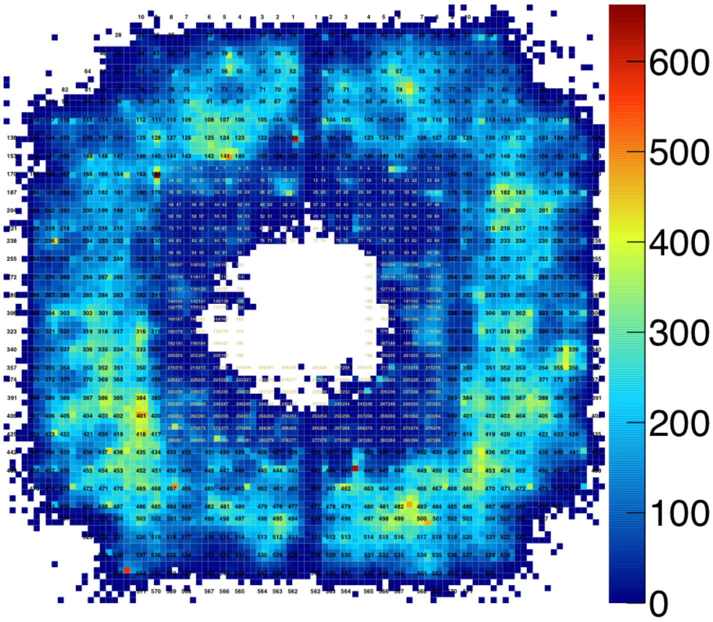

Figure 2.2: Example of EM-jet distribution at FMS after additional hot channel masking.

Chapter 3

Single Diffractive Process and Event Selection

One of the major characteristics of the diffractive processes is the presence of the rapidity gap. This analysis utilizes the proton track from east RP and the EM-jet at FMS, which allows for the large rapidity gap. Since there is only 1 proton in the final state process, this diffractive process is called the single diffractive process. The diagram for this process is shown in Fig. (3.1).

In order to determine the single diffractive process and minimize the effect of accidental coincidence events (AC) and pile-up events, the event selections and corrections include the following items:

1. Triggers: The triggers used for this analysis are the FMS BS triggers and FMS JP triggers. They are listed in Table(2.1). Only the events with any triggers fired are kept.
2. EM-jet cut: Details of the EM-jet cuts are in Section (3.1)
    - EM-jet reconstruction: EM-jets are reconstructed by FMS points

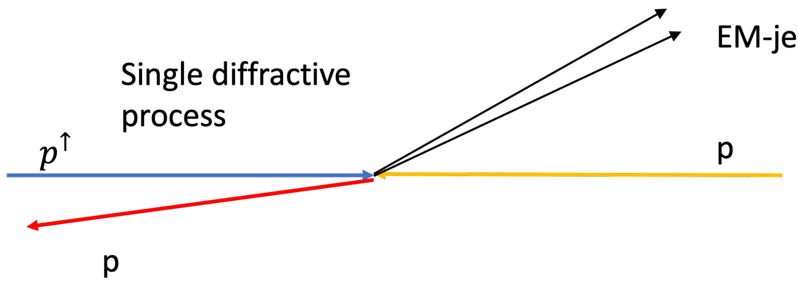

Figure 3.1: Diagram for single diffractive process.

  using the Anti-k_T algorithm with R = 0.7. The FMS points are required to have $E > 1$ GeV and $E_T > 0.2$ GeV.

- The EM-jets are required to have $p_T > 2$ GeV and pass trigger p_T threshold.
- The pseudorapidity (η) of the EM-jets is within [2.8, 3.8].
- The event with EM-jet $E > 100$ GeV are excluded.
- The number of EM-jets for each event is 1.
- Energy corrections for EM-jets: Underlying-Event (UE) correction (details in Sector(4.1) , and EM-jet energy correction (details in Sector(4.2)))

3. Event property cut: Details of the event property cuts are in Section (3.2)
    - Veto on abort gap.
    - The spin status for the blue beam and yellow beam is correct and accepts the 4 cases of 4-bit spin patterns (Tab. (3.2)).
    - The vertex z is within [-80, 80] cm.
4. BBC East veto cut: Details of the BBC East veto cut are in Section (3.3).
    - East BBC ADC sum cut: east side large BBC ADC sum < 80 and east side small BBC ADC sum < 90.
5. Roman Pot (RP) track cut: Details are in Section (3.4)
    - Only accept the event with exactly only one east side RP track.
    - The east RP track must hit at least 7 RP silicon planes.
    - East RP track ξ dependent θ_X, θ_Y, p_X and p_Y cuts.
    - East RP track ξ range: $0 < \xi < 0.15$

3.1 Electromagnetic jet reconstruction and cuts

Electromagnetic jets (EM-jets) are jets consisting of only photons. The photon candidates for EM-jets reconstruction are the FMS points. The description of FMS points can be found in [14].

In order to reduce the noise background, only the FMS points with $E > 1$ GeV are applied to the EM-jet reconstruction. The EM-jets are reconstructed with the anti-k_T algorithm from the FastJet package [13], with the resolution parameter $R = 0.7$. The primary vertex of the EM-jets is determined according to the priority of the TPC vertex, VPD vertex, and BBC vertex. If the primary vertex cannot be determined among these three detectors, it will be set to be (0,0,0). The EM-jet transverse momentum (p_T) is required to pass the trigger threshold and the fixed threshold 2 GeV/c threshold. The trigger thresholds are listed in Table (3.1). All of them have a 15% increase compared to the original trigger threshold setup.

The EM-jet vertex is determined by the primary vertex following the priority of TPC, VPD, and BBC. If the primary vertex can be obtained by TPC, the TPC vertex will be the primary vertex. Otherwise, check the VPD vertex on the next step. If there is no VPD vertex, then check the BBC vertex. If there is still no BBC vertex, the primary vertex is set to be z=0. The fraction of the vertex z obtained from TPC, VPD, and BBC are 1%, 33%, and 50%, respectively. The vertex z cut on $|z| < 80$ cm is considered.

In addition, we apply the cut on EM-jet pseudorapidity (η), which aims to get rid of the badly reconstructed EM-jets and the EM-jets hitting outside the FMS. Therefore, the η of the EM-jet cut is required to be within [2.8, 3.8].

Also, the events with EM-jet energy $E > 100$ GeV or $|x_F| > 1$ are discarded, where Feynman-x x_F can be estimated by the EM-jet energy divided by the beam energy ($x_F = \frac{2E}{\sqrt{s}}$). These events are about 0.17% of the entire dataset. Those events with these unreasonable EM-jets are possibly pile-up events.

The general raw EM-jet p_T vs energy distribution is shown in Fig. (3.2).

Finally, the number of EM-jets in each event is required to be only one. This can satisfy the requirement for single diffractive events and minimize the effect of the pile-up events. Figure (3.3) shows the number of EM-jets distribution, about 92% of the events are containing only one EM-jet at FMS.

3.2 Event property cut

The abort gap for both blue beam and yellow beam is within bunch ID [31, 39] and [111, 119] for run 15. The events with either blue beam or yellow beam with the abort gap are discarded.

The spin patterns for each beam, either up or down, are obtained from the bunch crossing of each event. The translation from the database for the spin patterns is described in Tab. (3.2). The spin patterns for both blue and yellow beam are combined as 4-spin bit. The events satisfying the following 4 4-spin bit cases in Table (3.2) are considered in this analysis. These patterns require the polarizations of both blue and yellow beam are either up or down.

Trigger name	Trigger ID	15% increase p_T cut [GeV]
FMS-JP0	480810 / 480830	1.84
FMS-JP1	480809 / 480829	2.76
FMS-JP2	480808 / 480828	3.68
FMS-sm-bs1	480801	1.26
FMS-sm-bs1	480821 / 480841	1.15
FMS-sm-bs2	480802 / 480822	1.84
FMS-sm-bs3	480803	2.53
FMS-sm-bs3	480823 / 480843	2.18
FMS-lg-bs1	480804	1.26
FMS-lg-bs1	480824 / 480844	1.15
FMS-lg-bs2	480405 / 480425	1.84
FMS-lg-bs3	480406 / 480426	2.76

Table 3.1: EM-jet trigger threshold p_T cut, listed by trigger name and trigger ID.

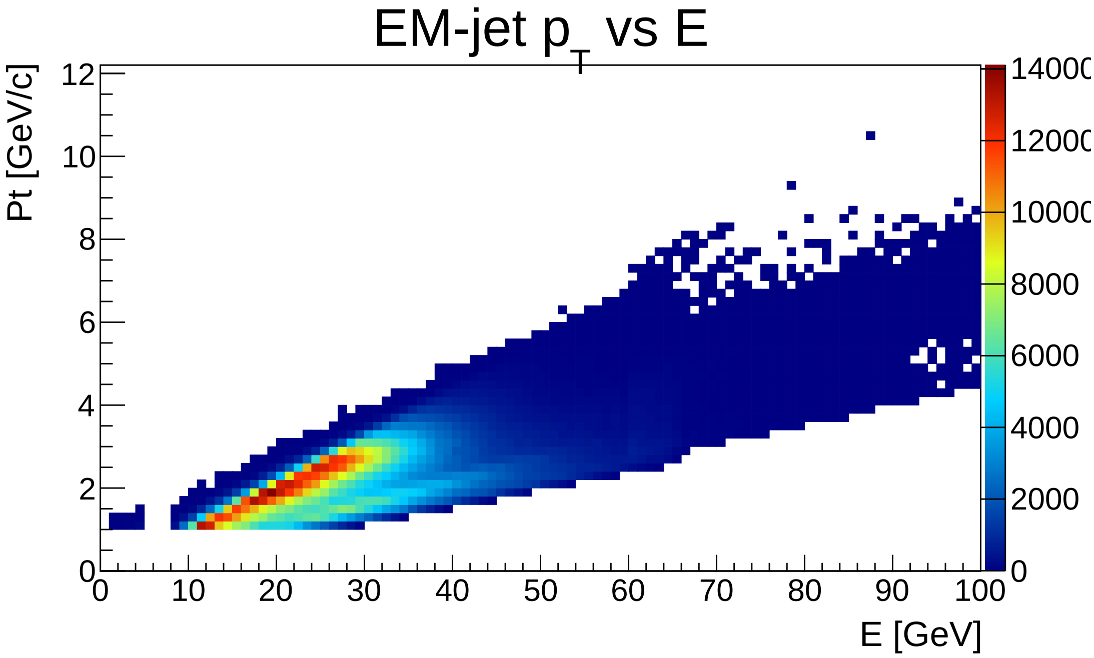

Figure 3.2: EM-jet transverse momentum (p_T) vs energy (E) before correction.

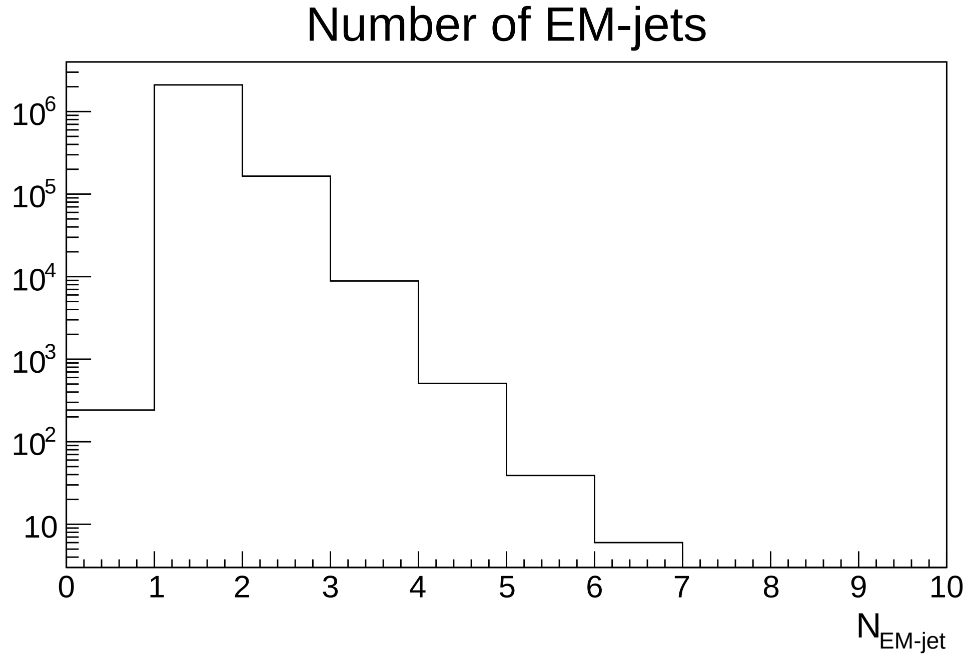

Figure 3.3: Number of EM-jets in the event.

Table 3.2: 4 acceptable 4-bit spin patterns

4-bit spin	Translate	Blue beam polarization	Yellow beam polarization
0101	5	up	up
0110	6	up	down
1001	9	down	up
1010	10	down	down

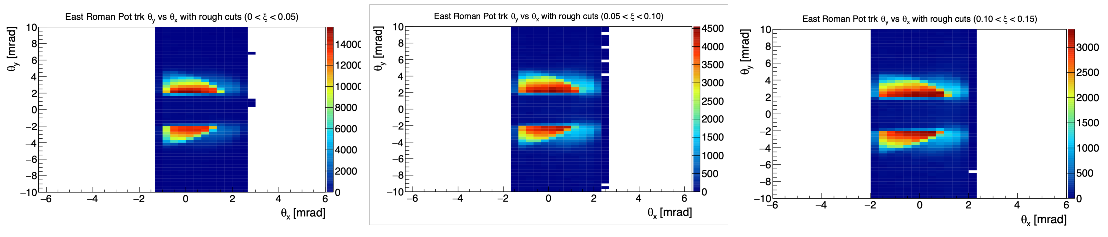

Figure 3.4: East RP θ_X and θ_Y distributions for 7 different East RP track ξ ranges with only applying East BBC ADC sum < 150.

3.3 BBC East veto cut

The major goal for the BBC East veto cut is to minimize accidental coincidence events (AC), also called multiple collision events. Furthermore, it helps to ensure the rapidity gap requirement for the single diffractive process since the BBC East detector covers $-5 < \eta < -2.1$.

The study of BBC East veto cuts is carried out simultaneously with the East RP track cut study. To begin with, the rough cut on a small BBC East ADC sum < 150 is applied to get rid of some of the backgrounds because the events with high BBC East ADC sum are more likely to be AC events. Then, with the rough BBC East ADC sum cut, the East RP θ_X and θ_Y distributions for East RP track with different ξ ranges are checked, where ξ is the fraction of proton momentum loss in the collision. The goal of checking the rough East RP θ_X and θ_Y distributions is to figure out the rough East RP θ_X and θ_Y cuts and use them to further checking the proper small/large BBC East ADC sum distribution to determine the BBC East veto cuts. Figure (3.4) shows the rough East RP θ_X and θ_Y distributions for 7 different East RP ξ regions. From the hot areas for every single figure, which are shown in red and yellow color, we determine the rough cut for East RP θ_X and θ_Y. The rough East RP θ_Y cuts are: $2.0 < |\theta_Y| < 4.0$ mrad, and The rough East RP θ_X cuts are shown in Tab. (3.3). Then, with the rough East RP θ_X and θ_Y cuts applied, we explore the small/large east BBC ADC sum distributions to determine the cuts on small/large east BBC cuts. The left panel of Fig. (3.5) shows the small east BBC ADC sum distribution, while the right panel of Fig. (3.5) shows the large east BBC ADC sum distribution. According to Fig. (3.5), we decide the small BBC east ADC sum < 90 and the large BBC east ADC sum < 80.

3.4 Roman Pot track cut

The proton track is detected from the RP detector, where the description of the RP detector can be found in [15]. For this analysis, we only accept the case with

ξ range	θ_X rough cuts [mrad]
$0.00 < \xi < 0.05$	$-1.0 < \theta_X < 1.5$
$0.05 < \xi < 0.10$	$-1.25 < \theta_X < 1.25$
$0.10 < \xi < 0.15$	$-1.5 < \theta_X < 1.25$
$0.15 < \xi < 0.20$	$-2.0 < \theta_X < 0.75$
$0.20 < \xi < 0.25$	$-2.5 < \theta_X < 0.75$
$0.25 < \xi < 0.30$	$-3.0 < \theta_X < 0.5$
$0.30 < \xi < 0.50$	$-5.0 < \theta_X < -0.25$

Table 3.3: Rough cuts for East RP track θ_X by different East RP track ξ

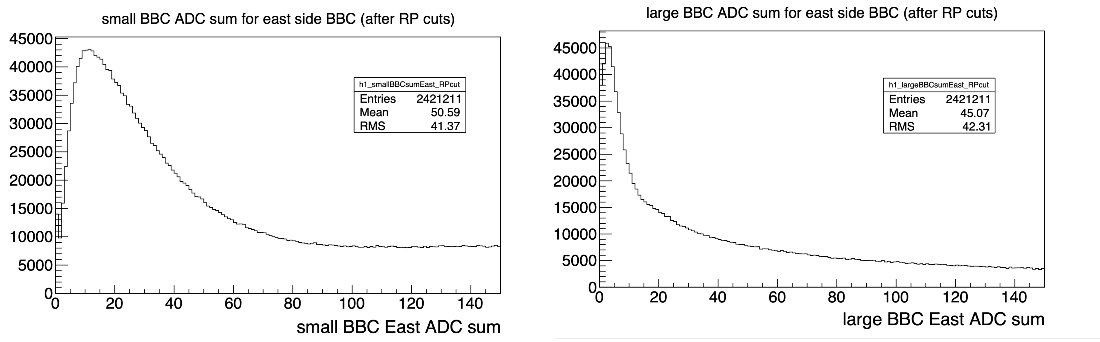

Figure 3.5: The small (left) and large (right) East BBC ADC sum distribution after the rough East RP θ_X and θ_Y cuts

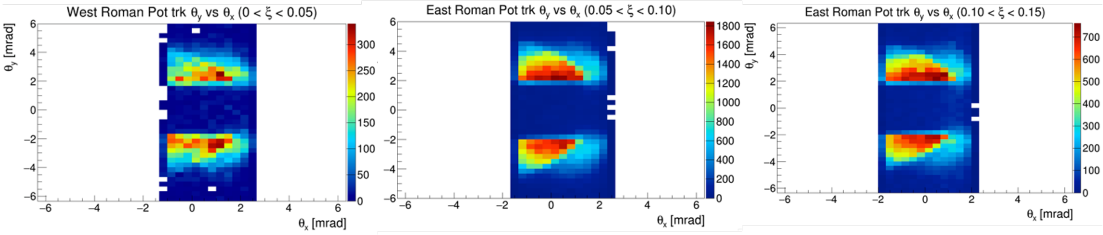

Figure 3.6: East RP θ_X and θ_Y distributions for three East RP track ξ ranges.

ξ range	θ_X final cuts [mrad]
$0.00 < \xi < 0.05$	$-1.0 < \theta_X < 1.5$
$0.05 < \xi < 0.10$	$-1.25 < \theta_X < 1.25$
$0.10 < \xi < 0.15$	$-1.5 < \theta_X < 1.25$

Table 3.4: Final cuts for East RP track θ_X by three ξ regions

only one East RP track detected. To ensure the RP track is well reconstructed, the RP track must hit at least 7 RP silicon planes. Also, the BBC East veto cuts (details in Sec. (3.3)) are also applied to explore the East RP track cuts. Furthermore, according to the Particle Data Book [16], the proton ξ for the diffractive process should be less than 0.15. Therefore, the cut on East RP track $0 < \xi < 0.15$ is also applied. With all of these cuts applied, first of all, the East RP track θ_X and θ_Y distributions are further explored. Figure (3.6) shows the East RP track θ_X and θ_Y distributions for three ξ ranges. The hot area will be considered as acceptable final East RP θ_X and θ_Y cuts. The final East RP track θ_Y cuts are uniform for all three ξ ranges: $2 < |\theta_Y| < 4$ mrad. However, the final East RP track θ_X cuts are ξ dependent, shown in Tab. (3.4). Finally, with then the final East RP θ_X and θ_Y cuts applied, the East RP track p_X and p_Y distributions are also explored to study their cuts. The idea is the same as investigating the East RP track θ_X and θ_Y cuts. Figure (3.7) shows the East RP track p_X and p_Y distributions for three ξ ranges. The shape of a rectangle with a quarter circle is used to describe the final East RP track p_X and p_Y cuts. The expressions are detailed in Tab. (3.5).

In summary, the cuts on East RP track include all the following: Number of RP Silicon planes hits greater than 6; $0 < \xi < 0.15$; East RP track θ_X and θ_Y cuts; East RP track p_X and p_Y cuts.

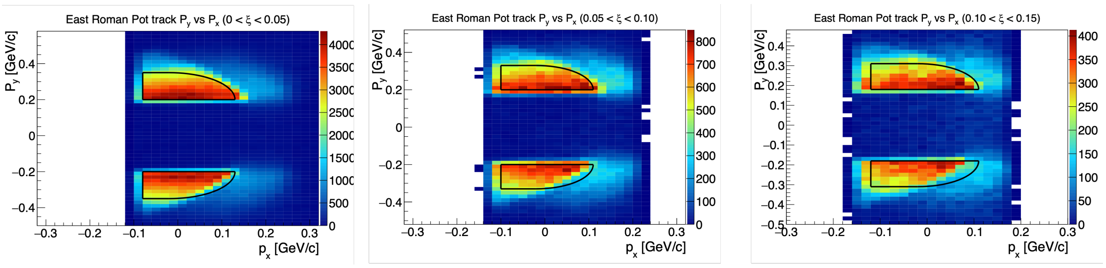

Figure 3.7: East RP track p_X and p_Y distributions for three East RP track ξ ranges. The black curves indicate the ranges of accepted East RP track p_X and p_Y cuts.

ξ range	p_X and p_Y final cuts [GeV/c]
$0.00 < \xi < 0.05$	$(p_X + 0.02)^2 + (\lvert p_Y\rvert - 0.2)^2 < 0.15^2$ or $-0.08 < p_X < -0.02$ and $0.2 < \lvert p_Y\rvert < 0.35$
$0.05 < \xi < 0.10$	$(p_X + 0.02)^2 + (\lvert p_Y\rvert - 0.2)^2 < 0.13^2$ or $-0.10 < p_X < -0.02$ and $0.2 < \lvert p_Y\rvert < 0.33$
$0.10 < \xi < 0.15$	$(p_X + 0.02)^2 + (\lvert p_Y\rvert - 0.18)^2 < 0.13^2$ or $-0.12 < p_X < -0.02$ and $0.18 < \lvert p_Y\rvert < 0.31$

Table 3.5: East RP track p_X and p_Y final cuts

Chapter 4

Corrections

4.1 Underlying Event (UE) correction

The underlying event contribution is part of a jet, not from the parton fragmentation but from secondary scattering or other processes. This will deposit some energy into the jet, so the correction on UE is required to subtract its energy from the jet. The "off-axis" method [17] is used. In this method, first of all, two off-axis jets with the same pseudorapidity but at $\pm\pi/2$ azimuthal angle at the edge of the original jet are reconstructed as UE background. Then, the UE energy density (ρ) can be calculated using $\rho = E/(\pi R^2)$, where E is the average UE energy and R is the UE jet radius. The fastjet program uses the "ghost particle" technique to calculate the jet area (A). The maximum "ghost particle" η is 5.0, and the "ghost area" is 0.04. Finally, the jet energy will be subtracted by the UE energy: $E_{corrected} = E_{original} - \rho \times A$, where the corrected EM-jet energy is $E_{corrected}$, and the original EM-jet energy is $E_{original}$.

Figure (4.1) shows the UE correction distribution for EM-jet energy. The left plot shows the subtraction term for the UE correction for EM-jet energy. The right plot shows the EM-jet energy distribution after the UE correction. If the EM-jet energy after subtraction is less than 0 GeV, the energy will be set to 0 GeV.

4.2 Detector level to particle level EM-jet energy correction

The EM-jet energy obtained from FMS is considered detector-level EM-jet energy. Therefore, a correction for detector level to particle level EM-jet energy is necessary. The correction is based on the Monte Carlo simulation for FMS. For

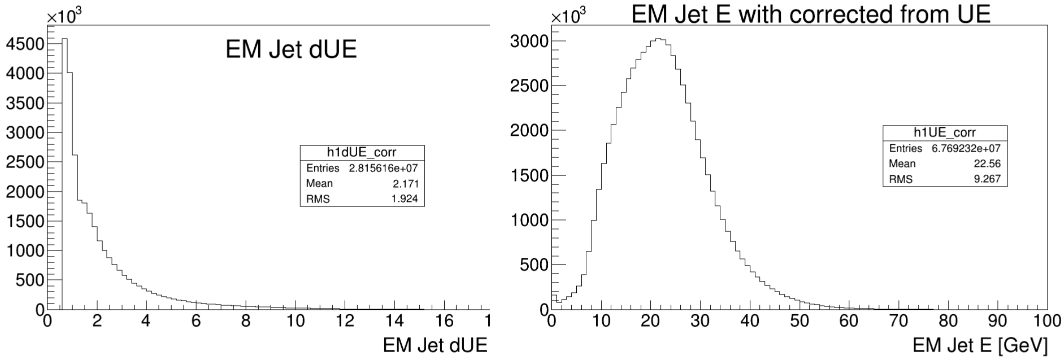

Figure 4.1: UE distribution for diffractive EM-jet analysis. The left plot shows the subtraction term $\rho \times A$. The right plot shows the EM-jet energy distribution after the UE correction.

the PYTHIA simulation, the proton-proton collisions with $\sqrt{s} = 200$ GeV are generated, with the tune setting of Perugia2012 (Tune parameter 370) [18, 19]. Then, the GEANT3 with FMS detector response implemented under STAR simulation framework ("starsim") is used for the FMS simulation. The Big Full Chain (BFC) proceeds with the event reconstruction. The chain options are "ry2015a agml usexgeom MakeEvent McEvent vfmce Idst BAna l0 l3 Tree logger fmsSim fmspoint evout -dstout IdTruth bigbig fzin geantout clearmem sdt20150417.193427". The EM-jet reconstruction is proceeded along with the BFC process. The Anti-k_T algorithm with R=0.7 is used for the EM-jet reconstruction, the same as the EM-jet reconstruction for data.

For the simulation results, the EM-jets with both particle level and detector level are recorded. Figure (4.2) shows the EM-jet energy distribution in particle level (y-axis) and detector level (x-axis). Figure (4.3) shows the profile of the EM-jet energy distribution with particle level and detector level. The black points are the correlation between the EM-jet energy at the particle level and detector level. The red curves are fit for the points in two different detector level regions: $5 < E < 10$ GeV and $10 < E < 60$ GeV. The 6th-order polynomial function is used for fitting the former region and the linear function is used for fitting the latter region. The parameters of the 6th-order polynomial are shown in Tab. (4.1), while the linear function is: $E_{par} = 1.07 * E_{det} + 1.13$, where E_{par} is the particle level EM-jet energy and E_{det} is the detector level EM-jet energy. These functions are used to calculate the corrected energy from the original detector level energy. The corrected EM-jet energy will finally applied for the x_F calculation and A_N extraction.

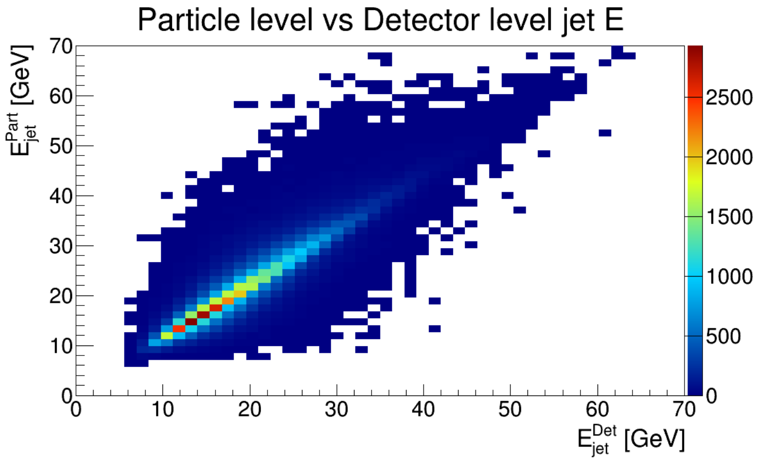

Figure 4.2: EM-jet energy distribution in particle level (y-axis) and detector level (x-axis) from the FMS simulation.

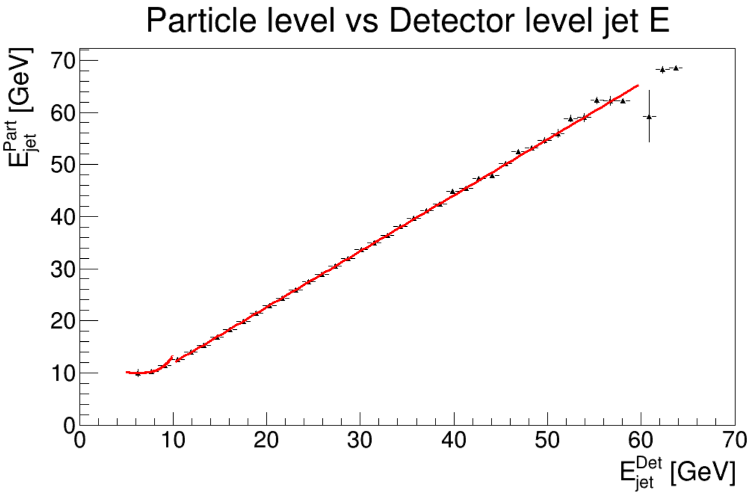

Figure 4.3: The profile of the EM-jet energy distribution with particle level and detector level. The black points are the correlation between the EM-jet energy at the particle level and detector level. The red curves are the fit for the black points.

[0]	[1]	[2]	[3]	[4]	[5]	[6]
8.93e0	-6.64e-1	1.51e-1	-6.66e-3	1.56e-4	-1.85e-6	8.65e-9

Table 4.1: Parameters for the 6th-order polynomial

Chapter 5

Rapidity Gap (RG) events study

5.1 Motivation

The rapidity gap (RG) events are also within our interest in studying the potential background for the single diffractive events. The RG events are the type of events coinciding with FMS EM-jets and East BBC veto, with the schematic diagram shown in Fig. (5.1). The details description for the FMS EM-jets and east BBC veto are in Sec. (5.2). Since there is no requirement on the RP track (proton) on any side, the RG events are considered as the subset of the inclusive events, and they can also serve as additional enrichment for the inclusive process. According to the Pythia 8 simulation for hard QCD process (can be considered as non-single diffractive events) and the single diffractive events, the east BBC veto cuts are able to cut out about 84% of the non-single diffractive events, but just cut out about 14% of the single diffractive events with a proton on the east side. If considering the present of the jet in the FMS region, the BBC veto rate for the NSD events can be higher up to 99%. Therefore, such a process can help separate the diffractive and non-diffractive processes with the rapidity gap requirement. Studying the RG events can allow us to investigate the single diffractive process without the effects on the limited Roman Pot acceptance for tagging the scattered proton.

5.2 Event selection for RG events

The dataset used for the RG events is the same as single diffractive events, shown in Sec. (2.1). The event selection criteria of the FMS EM-jets, event

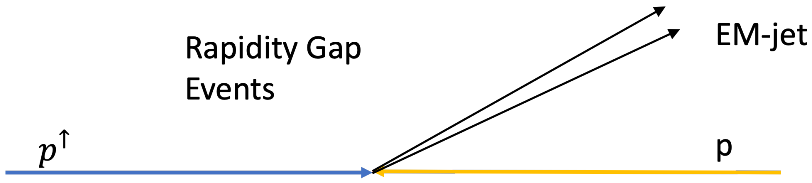

Figure 5.1: Diagram for rapidity gap events.

property cuts, and the East BBC veto for the RG events are the same as those for the single diffractive events, which are shown in Sec. (3.1), Sec. (3.2) and Sec. (3.3), respectively. The idea behind choosing the same FMS EM-jet cuts and East BBC veto cuts is to make them consistent and comparable to the single diffractive process.

5.3 Fraction of single diffractive events in rapidity gap events

The study on the fraction of single diffractive events in rapidity gap events in data can be measured using the simulation. The simulation is using the Pythia 8 single diffractive process (SoftQCD:singleDiffractive). Both the east BBC detector simulation (via GEANT3 based STAR detector level simulation) and the east RP detector simulation (via pp2pp simulation [25]) are used for the simulation study. The same east BBC veto (detailed in Sec. (3.3)) is applied in the simulation to determine the veto on the east BBC region (rapidity gap) as well. The cut on the east RP track hitting more than 6 east RP planes is used for determining the good east RP track. In addition, only one RP track is allowed as the east RP cut for the single diffractive events.

Based on the criteria above, we define the single diffractive events (SD) in the simulation as the events passing the east BBC veto and the east RP cut. Also, we define the rapidity gap events (RG) in the simulation as the events passing the east RP cut without requirement on the east RP cut. The RG events in simulation are all real single diffractive events (RSD). The definition of single diffractive events and rapidity gap events in data are the same as mentioned in previous sections. However, the RG events in data contain real single diffractive events (RSD) and non-single diffractive events (NSD). When we calculate the fraction of single diffractive events to the rapidity gap events in simulation and data, the equation for simulation and data can be expressed as Equ. (5.1) and Equ. (5.2), respectively. In the calculation, $frac(sim) = 16.03\%$ and $frac(data) = 11.08\%$. Since the purity of the single diffractive events in data is high, we can consider the fraction of single diffractive events (SD) to the real single diffractive events in rapidity gap event (RSD), $\frac{SD}{RSD}$, is same between data and simulation. Considering the major systematic uncertainty of the fraction comes from the uncertainty of BBC detector (6.5%) [26] and RP detector (10%) [25]. The SD fraction in RG events in data ($\frac{RSD}{RSD+NSD}$) is $68.7\% \pm 0.6\% \pm 8.2\%$.

$$frac(sim) = \frac{SD}{RSD} \tag{5.1}$$

$$frac(data) = \frac{SD}{RSD + NSD} \tag{5.2}$$

Chapter 6

Semi-exclusive process study

The semi-exclusive process requires only one EM-jet at FMS and one proton detected in west side RP. The event selections of the EM-jet are same as that used in single diffractive process and rapidity gap events, showing in Sec. 3.1. Additionally, an exclusive constraint on the sum of the energy of the EM-jet and the west RP track (energy sum) is applied. It requires the energy sum are same as proton beam energy within resolution. Therefore, this process is termed as semi-exclusive process. The schematic diagram for semi-exclusive process is shown in Fig. (6.1).

In order to determine the semi-exclusive process and minimize the effect of accidental coincidence events (AC) and pile-up events, the event selections and corrections include the following items:

1. Triggers: The triggers used for this analysis are the FMS BS triggers and FMS JP triggers. They are listed in Table(2.1). Only the events with any triggers fired are kept.

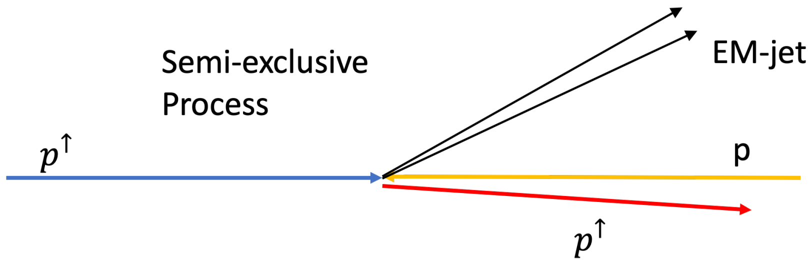

Figure 6.1: Diagram for semi-exclusive process.

2. EM-jet cut: Details of the EM-jet cuts are in Section (3.1) These cuts are same as that in single diffractive process and rapidity gap events.
    - EM-jet reconstruction: EM-jets are reconstructed by FMS points using the Anti-k_T algorithm with R = 0.7. The FMS points are required to have $E > 1$ GeV and $E_T > 0.2$ GeV.
    - The EM-jets are required to have $p_T > 2$ GeV and pass trigger p_T threshold.
    - The pseudorapidity (η) of the EM-jets is within [2.8, 3.8].
    - The event with EM-jet $E > 100$ GeV are excluded.
    - The number of EM-jets for each event is 1.
    - Energy corrections for EM-jets: Underlying-Event (UE) correction (details in Sector(4.1) , and EM-jet energy correction (details in Sector(4.2)))
3. Event property cut: Details of the event property cuts are in Section (3.2)
    - Veto on abort gap.
    - The spin status for the blue beam and yellow beam is correct and accepts the 4 cases of 4-bit spin patterns (Tab. (3.2)).
    - The vertex z is within [-80, 80] cm.
4. BBC West veto cut: Details of the BBC West veto cut are in Section (6.1).
    - West BBC ADC sum cut: west side large BBC ADC sum < 60 and west side small BBC ADC sum < 80.
5. Roman Pot (RP) track cut: Details are in Section (6.2)
    - Only accept the event with exactly only one west side RP track.
    - The west RP track must hit at least 7 RP silicon planes.
    - West RP track ξ dependent θ_X, θ_Y, p_X and p_Y cuts.
    - West RP track ξ range: $0 < \xi < 0.45$
6. Energy sum cuts: Sum of the energy of west RP track and EM-jet is required to be equal to the beam energy, within the resolution.

6.1 West BBC veto cuts

The major goal for the BBC West veto cut is to minimize accidental coincidence events (AC), which are called multiple collision events. However, the west BBC

West RP ξ range	West RP θ_X rough cut [mrad]
$0 < \xi < 0.05$	$-1 < \theta_X < 1.75$
$0.05 < \xi < 0.1$	$-1.5 < \theta_X < 1.5$
$0.1 < \xi < 0.15$	$-1.75 < \theta_X < 1.25$
$0.15 < \xi < 0.2$	$-2.5 < \theta_X < 1.25$
$0.2 < \xi < 0.25$	$-3 < \theta_X < 1$
$0.25 < \xi < 0.3$	$-3.25 < \theta_X < 0.5$
$0.3 < \xi < 0.35$	$-3.75 < \theta_X < 0$
$0.35 < \xi < 0.4$	$-4.25 < \theta_X < -0.5$
$0.4 < \xi < 0.45$	$-5 < \theta_X < -1$

Table 6.1: Rough west RP θ_X cuts

coverage is partially overlapped with the FMS coverage. Therefore, this west BBC veto can not provide enough size of rapidity gap to satisify the requirement of the diffractive process.

The idea for determining the west BBC veto cuts are similar as for determining the east BBC veto cuts. To begin with, the rough cuts on west RP θ_X and θ_Y are applied to check the small BBC west ADC sum distribution. The distribution of west RP θ_Y vs θ_X are showing in Fig.(6.2), with the rough cut on west small BBC ADC sum < 150. From the plots, we determine the rough west RP θ_Y cut on: $1.5 < |\theta_Y| < 4$ mrad, with the rough west RP θ_X cuts are listed in Tab. (6.1).

With these rough west RP θ_X and θ_Y cuts, the small BBC west ADC sum and the large BBC west ADC sum distributions are then checked. Figure (6.3) shows the small BBC west ADC sum, and Fig. (6.4) shows the large BBC west ADC sum. From the plots, we apply the cuts on small BBC west ADC sum < 80 and large BBC west ADC sum < 60.

6.2 Roman Pot (RP) track cut

The proton track for semi-exclusive process is detected from the west side RP detector. Only one west side RP track is accepted for this process, with no constrain on east side tracks. In addition, this west side RP track requires to hit more than 6 planes. The first set of cuts are the west RP θ_X and θ_Y cuts. Before exploring these cuts, the west BBC veto cuts are applied. Figure (6.5) shows the final distribution of west RP θ_Y vs θ_X. From the distributions, we

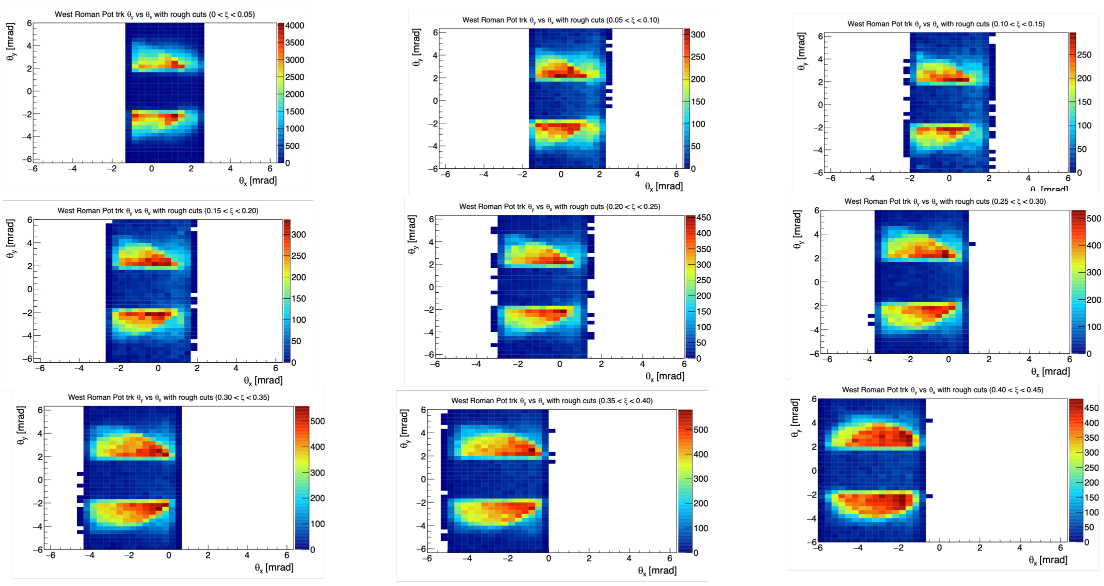

Figure 6.2: West RP θ_X and θ_Y distributions for 9 different East RP track ξ ranges with only applying West BBC ADC sum < 150.

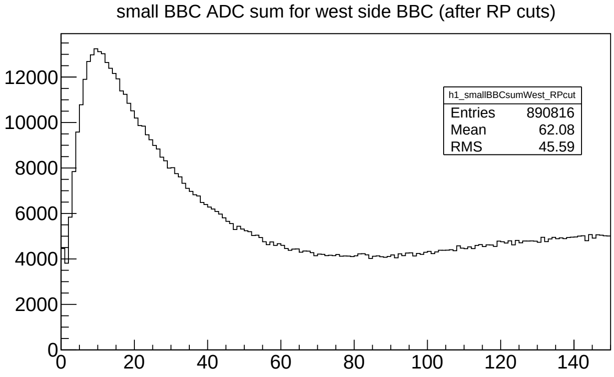

Figure 6.3: Small BBC west ADC sum distribution after the rough west RP cuts.

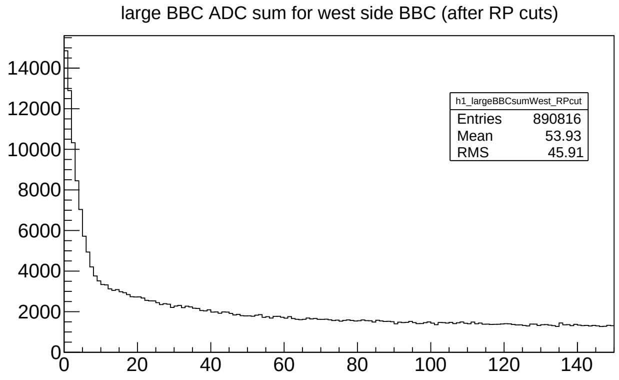

Figure 6.4: Large BBC west ADC sum distribution after the rough west RP cuts.

determine the θ_Y cuts on: $1.5 < |\theta_Y| < 4$ [mrad] ; and the θ_X cuts shown in Tab. (6.2). Then, with applying the west RP θ_X and θ_Y cuts, the west RP p_X and p_Y cuts are explored. Figure (6.6) shows the final distribution of west RP θ_X and θ_Y with the black curve region indicating the ranges of the cuts. The cut values are shown in Tab. (6.3).

6.3 Energy sum cuts

For the semi-exclusive process, the final state includes the EM-jet and the proton. Both are on the same side (west side). Therefore, an exclusive constrain on the sum of the energy for EM-jet and the proton should be consistent with the beam energy within resolution. This is the reason for naming this process as semi-exclusive process.

The energy sum cuts are explored with applying the west BBC veto cuts and the west RP cuts. They are shown with EM-jet x_F dependent in Fig. (6.7). and in Tab. (6.4).

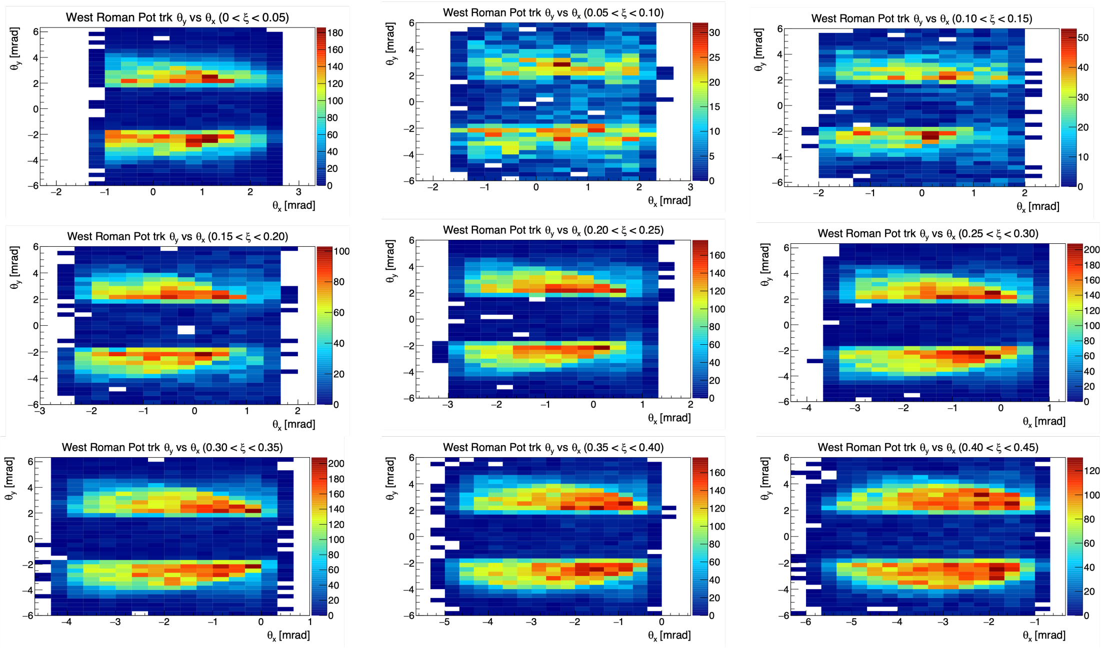

Figure 6.5: West RP θ_X and θ_Y distributions for 9 different East RP track ξ ranges after applying West BBC veto cuts.

West RP ξ range	West RP θ_X final cut [mrad]
$0 < \xi < 0.05$	$-1 < \theta_X < 1.75$
$0.05 < \xi < 0.1$	$-1.5 < \theta_X < 1.5$
$0.1 < \xi < 0.15$	$-1.75 < \theta_X < 1.25$
$0.15 < \xi < 0.2$	$-2 < \theta_X < 1$
$0.2 < \xi < 0.25$	$-2.75 < \theta_X < 0.5$
$0.25 < \xi < 0.3$	$-3.25 < \theta_X < 0.5$
$0.3 < \xi < 0.35$	$-3.75 < \theta_X < 0$
$0.35 < \xi < 0.4$	$-4.5 < \theta_X < -0.5$
$0.4 < \xi < 0.45$	$-5.5 < \theta_X < -1.25$

Table 6.2: Final west RP θ_X cuts

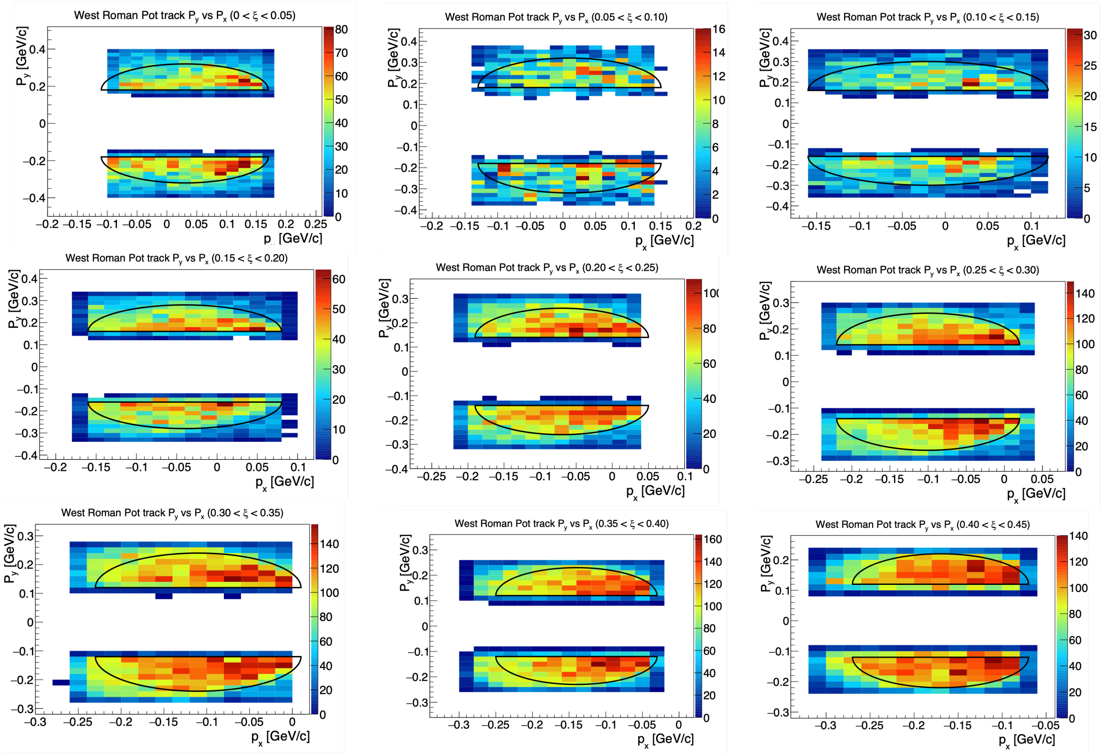

Figure 6.6: West RP track p_X and p_Y distributions for nine West RP track ξ ranges. The black curves indicate the ranges of accepted West RP track p_X and p_Y cuts.

West RP ξ range	West RP p_X and p_Y final cut [GeV/c]
$0 < \xi < 0.05$	$(p_X - 0.03)^2 + (p_Y - 0.18)^2 < 0.14^2$ and $0.18 < \lvert p_Y \rvert < 0.32$
$0.05 < \xi < 0.1$	$(p_X - 0.01)^2 + (p_Y - 0.18)^2 < 0.14^2$ and $0.18 < \lvert p_Y \rvert < 0.32$
$0.1 < \xi < 0.15$	$(p_X + 0.02)^2 + (p_Y - 0.16)^2 < 0.14^2$ and $0.16 < \lvert p_Y \rvert < 0.3$
$0.15 < \xi < 0.2$	$(p_X + 0.04)^2 + (p_Y - 0.16)^2 < 0.12^2$ and $0.16 < \lvert p_Y \rvert < 0.28$
$0.2 < \xi < 0.25$	$(p_X + 0.07)^2 + (p_Y - 0.14)^2 < 0.12^2$ and $0.14 < \lvert p_Y \rvert < 0.26$
$0.25 < \xi < 0.3$	$(p_X + 0.1)^2 + (p_Y - 0.14)^2 < 0.12^2$ and $0.14 < \lvert p_Y \rvert < 0.26$
$0.3 < \xi < 0.35$	$(p_X + 0.11)^2 + (p_Y - 0.12)^2 < 0.12^2$ and $0.12 < \lvert p_Y \rvert < 0.24$
$0.35 < \xi < 0.4$	$(p_X + 0.14)^2 + (p_Y - 0.12)^2 < 0.11^2$ and $0.12 < \lvert p_Y \rvert < 0.23$
$0.4 < \xi < 0.45$	$(p_X + 0.17)^2 + (p_Y - 0.12)^2 < 0.1^2$ and $0.12 < \lvert p_Y \rvert < 0.22$

Table 6.3: Final west RP p_X and p_Y cuts

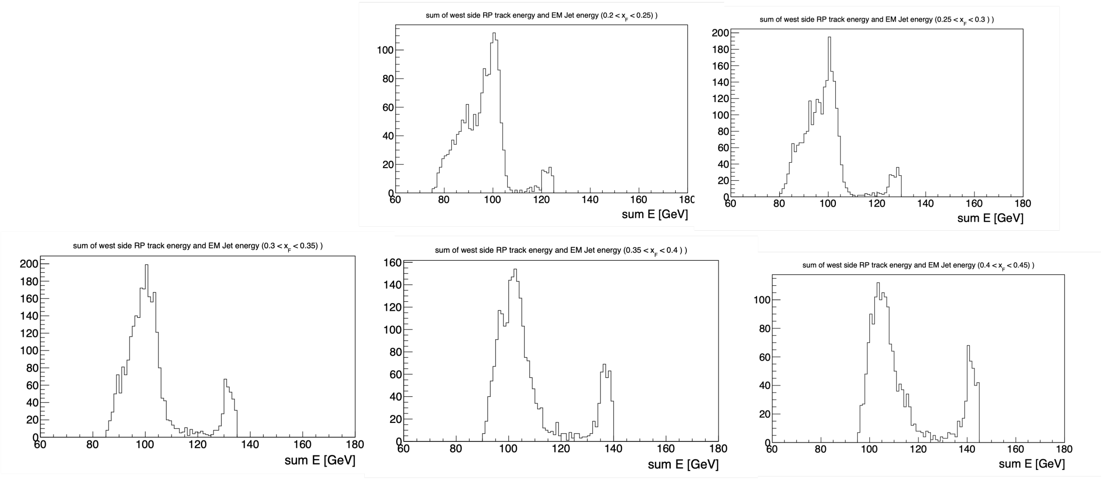

Figure 6.7: Energy sum cuts for 5 different EM-jet x_F regions

EM-jet x_F	Energy sum (E_{sum}) cut
0.2 - 0.25	$E_{sum} < 110$ GeV
0.25 - 0.3	$E_{sum} < 110$ GeV
0.3 – 0.35	$E_{sum} < 115$ GeV
0.35 – 0.4	$E_{sum} < 115$ GeV
0.4 – 0.45	$E_{sum} < 120$ GeV

Table 6.4: Energy sum cuts for semi-exclusive process

Chapter 7

Background study

7.1 Zerobias event study

The Zerobias events are the highly scaled events with the zerobias trigger. The details for the events are shown below:

- Trigger setup name: production_pp200trans_2015
- Data stream: zerobias
- Production tag: P16id

Since there are only a small fraction of events containing good EM-jets at the FMS, the Zerobias events are only used to estimate the accidental background for the analysis. To begin with, the NanoDst files are generated from the MuDst files. For the Zerobias events, there are no requirement on the EM-jets on FMS and no requirement on RP track. Then, the BBC East veto cuts (detailed in Sec. (3.3) and East RP track cuts (detailed in Sec. (3.4)) are applied to the Zerobias events, where both cuts are the same as single diffractive process. About 0.2% of the events pass the cuts mentioned above. Therefore, about 0.2% of the events are accidental coincidences and should be the same rate for every process.

With the Zerobias events, we also estimate the accidental coincidences (AC) for the measured single diffractive process. The AC events are coming from the situation that the FMS EM-jets and the east RP tracks are not correlated. For example, the FMS EM-jets and the east RP tracks are coming from multiple collisions, but they are recorded in one event in the data. Equation (7.1) shows the formula for calculating the fraction for the AC events. n_{AC} is the number of the AC events, but it is difficult to count directly. n_{mea} is the number of event counts per x_F bin in the asymmetry calculation for the single diffractive process. n_{RG} is the number of event counts per x_F bin in the asymmetry calculation for the RG events, where the description for RG events is in Sec. (5.1). $\frac{n_{AC}}{n_{RG}}$ can be considered as the AC events fraction for RG events, which is 0.2%. By counting the events per x_F bin for measured single diffractive process and RG events, the fraction for the AC events is about 1.8% for each x_F bin. This fraction is small, so its effect will be assigned to the systematic uncertainty, detailed in Appendix (B).

$$frac_{bkg} = \frac{n_{AC}}{n_{mea}} = \frac{n_{AC}}{n_{RG}} \times \frac{n_{RG}}{n_{mea}} \tag{7.1}$$

7.2 Mix event background for energy sum cut study

The energy sum cuts constrain the sum of the EM-jet energy and the west RP track energy. For the accidental coincidence (AC) in the semi-exclusive process, the energy sum is usually much higher than the beam energy because the west RP track is coming from the proton from the non-diffractive process, especially from the elastic scattering process. Therefore, in order to estimate the contribution to the semi-exclusive events from the AC events, the mix event background is studied to estimate such contribution.

For the mix event background study for energy sum, we use the distribution for the west RP track energy (momentum) in the zerobias event (7.1), and the distribution for the EM-jet energy from the inclusive process. The mix event energy sum background distribution is studied in different EM-jet x_F regions. The idea for the mix event energy sum background is to calculate all the possible combinations of the energy sum with west RP track momentum and EM-jet energy. Equation (7.2) shows the simple idea for the mix event energy sum calculation (Esum(i+j)). P(i) is the fraction of EM-jet yields in the inclusive EM-jet energy distribution for [i,i+1] (GeV) within the specific x_F range. n(j) is the yield in zerobias events west RP momentum distribution for [j,j+1] (GeV/c). Figure (7.1) shows one example of the mix event energy sum spectrum. In this example, The left panel of Fig. (7.1) shows the inclusive EM-jet energy spectrum for $0.2 < x_F < 0.25$, which corresponds to $20 <= i < 25$. The middle panel of Fig. (7.1) shows the zerobias events west RP momentum distribution, and only west RP momentum between 40 GeV and 100 GeV will be used for mix event background study, which corresponds to $40 <= j < 100$. The right panel of Fig. (7.1) show the energy sum distribution using the mix event background study for EM-jet with $0.2 < x_F < 0.25$.

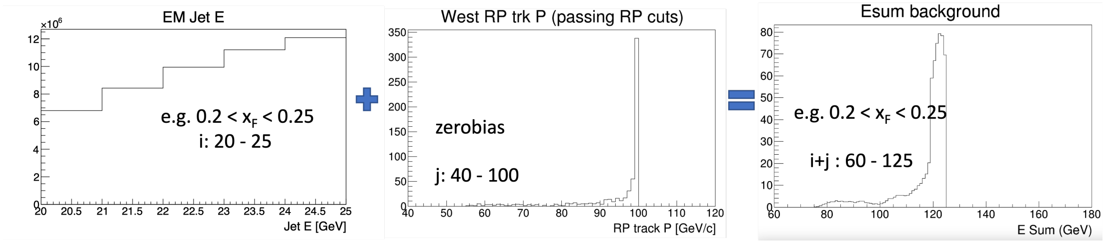

Figure 7.1: Example for mix event energy sum background study for EM-jet with $0.2 < x_F < 0.25$.

EM-jet x_F	Signal region [GeV]	Background region [GeV]
0.2 - 0.25	Esum $<$ 110 GeV	Esum $>$ 110 GeV
0.25 - 0.3	Esum $<$ 110 GeV	Esum $>$ 110 GeV
0.3 - 0.35	Esum $<$ 115 GeV	Esum $>$ 115 GeV
0.35 - 0.4	Esum $<$ 115 GeV	Esum $>$ 115 GeV
0.4 - 0.45	Esum $<$ 120 GeV	Esum $>$ 120 GeV

Table 7.1: Signal region and background region for energy sum spectrum in data

$$Esum(i+j) = \sum_{i,j} P(i) \times n(j) \tag{7.2}$$

Then, we use the shape of the mix event energy sum background to estimate its contribution to the semi-exclusive events. For the energy sum plots in data, we define the signal region and the background region based on the energy sum cut in Sec. (6.3). The signal region and the background region for each EM-jet x_F region are shown in Tab. (7.1). Then, the shape of the mix event energy sum background is scaled to the maximum bin value of the background region in each EM-jet x_F region. Figure (7.2) shows the mix event background results for each EM-jet x_F region. In each plot, the red curve indicates the energy sum distribution in data, while the black curve indicates the scaled mix event energy sum background. The fraction of the mix event energy sum background to the data can be calculated as the ratio of the integrated yields for the scaled mix event energy sum background within the signal region to the integrated yields for the data within the signal region. Table (7.2) shows this mix event energy sum background fraction. Since this fraction is small (less than 3%), we assign such fraction to the systematic uncertainty as the background term.

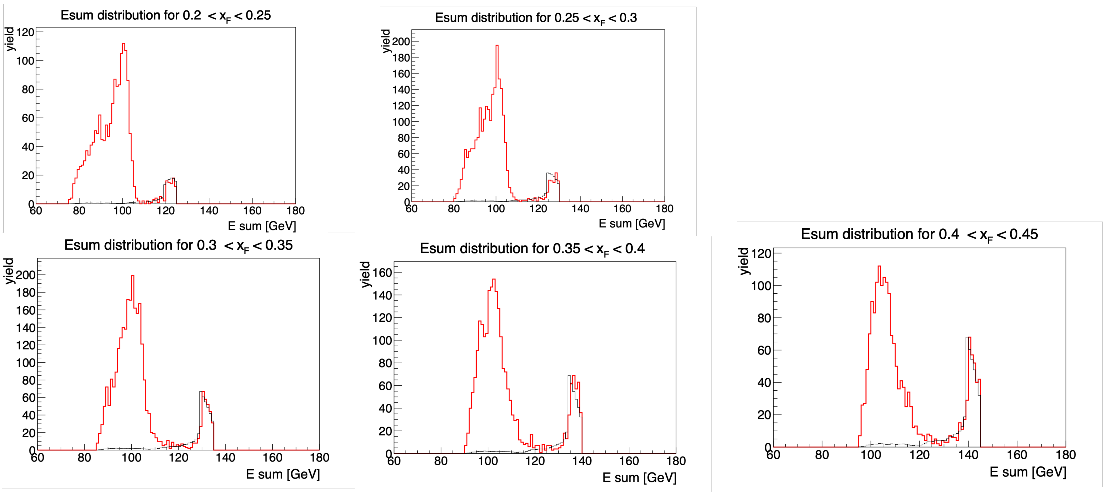

Figure 7.2: Mix event energy sum background study results for each EM-jet x_F regions. In each plot, the red curve indicates the energy sum distribution in data, while the black curve indicates the scaled mix event energy sum background.

x_F	Fraction of background (%)
0.2 - 0.25	1.3
0.25 - 0.3	1.3
0.3 - 0.35	2.1
0.35 - 0.4	2.0
0.4 - 0.45	2.7

Table 7.2: Fraction of the mix event energy sum background for each EM-jet x_F region

Chapter 8

Systematic Uncertainty for A_N

The systematic uncertainty for single diffractive process includes the cuts on East BBC veto cuts (details in 8.2), Ring of Fire (details in 8.3) and AC background (details in 7.1). The systematic uncertainty for rapidity gap events includes the cuts on East BBC veto cuts (details in 8.2) and Ring of Fire (details in 8.3). The systematic uncertainty for semi-exclusive process includes the cuts on West BBC veto cuts (details in 8.2), Ring of Fire (details in 8.3), energy sum cuts (details in 8.4) and AC background (details in 8.4).

8.1 Method for systematic uncertainty

To study the systematic uncertainty for the BBC veto cuts, Ring of Fire and the energy sum cuts the Bayesian method is applied [21]. For each term of systematic uncertainty study, we calculate the A_N standard deviation among the variation cuts. However, only the cuts with variations deemed significant would be included. If a cut with variations produces a maximum value with statistical uncertainty $A_N(1) \pm \delta_1$ and a minimum value with statistical uncertainty $A_N(2) \pm \delta_2$, only when $\frac{|A_N(1)-A_N(2)|}{\sqrt{|\delta_1^2-\delta_2^2|}} > 1$ the standard variation will be used for this systematic uncertainty term, otherwise this systematic uncertainty term will be assigned 0 (Barlow check) [21]. All the systematic uncertainty for each x_F bin will be calculated individually.

Variation	-20	-10	+10	+20
East Large BBC ADC sum cut	60	70	90	100
East Small BBC ADC sum cut	70	80	100	110
West Large BBC ADC sum cut	40	50	70	80
West Small BBC ADC sum cut	60	70	90	100

Table 8.1: List of BBC veto cut values for systematic uncertainty study.

8.2 Systematic uncertainty for the BBC veto cuts

The BBC veto cuts include East Large BBC ADC sum < 80 and East Small BBC ADC sum < 90, for the single diffractive process and the rapidity gap events. They also include West Large BBC ADC sum < 60 and West Small BBC ADC sum < 80, for the semi-exclusive process. We change the cut values for Large BBC and Small BBC ADC sum to study the systematic uncertainty, as shown in Tab. (8.1). We calculate the A_N with its statistical uncertainty for each cut standard variation with varying the cuts. Then, we use the Barlow check to determine whether to keep the standard derivation as systematic uncertainty [21]. Note, the systematic uncertainty for Large BBC and Small BBC ADC sum cuts are studied separately for each process.

8.3 Ring of Fire

The Ring of Fire is a kind of background related to the FMS-sm-bs3 trigger. This trigger is targeted at the inner region of FMS, which is close to the beam. It's generally recognized that the beam remnants are accepted by FMS-sm-bs3 trigger. Therefore, the effect of this trigger will be considered as one source of systematic uncertainty. The systematic uncertainty for the Ring of Fire will be the A_N result difference between considering this trigger and excluding this trigger. In addition, the Barlow check is applied to determine whether to keep the standard derivation as systematic uncertainty.

8.4 Energy sum cut uncertainty

To study the energy sum cut uncertainty, we varied the energy cut per x_F bin by ±10 GeV and ±5 GeV. Table (8.2) shows the exact values for studying the energy sum cut uncertainty. We calculate the A_N with its statistical uncertainty for each cut standard variation with varying these energy sum cuts. Then, we

EM-jet x_F	E_{sum} cut (-10 GeV)	E_{sum} cut (-5 GeV)	E_{sum} cut (+5 GeV)	E_{sum} cut (+10 GeV)
0.2 - 0.25	$E_{sum} < 100$ GeV	$E_{sum} < 105$ GeV	$E_{sum} < 115$ GeV	$E_{sum} < 120$ GeV
0.25 - 0.3	$E_{sum} < 100$ GeV	$E_{sum} < 105$ GeV	$E_{sum} < 115$ GeV	$E_{sum} < 120$ GeV
0.3 – 0.35	$E_{sum} < 105$ GeV	$E_{sum} < 110$ GeV	$E_{sum} < 120$ GeV	$E_{sum} < 125$ GeV
0.35 – 0.4	$E_{sum} < 105$ GeV	$E_{sum} < 110$ GeV	$E_{sum} < 120$ GeV	$E_{sum} < 125$ GeV
0.4 – 0.45	$E_{sum} < 110$ GeV	$E_{sum} < 115$ GeV	$E_{sum} < 125$ GeV	$E_{sum} < 130$ GeV

Table 8.2: Energy sum cuts for semi-exclusive process in the energy sum cut uncertainty study

use the Barlow check to determine whether to keep the standard derivation as systematic uncertainty [21].

8.5 Polarization uncertainty

The blue beam and yellow beam polarization are used to calculate the A_N results. As a habit, the uncertainty of beam polarization uncertainty is listed independently. The beam polarization measurement results are provided by the CNI group, which develops, maintains, and operates the RHIC polarimeter measurement. The beam polarization measurement results are listed in the table on the webpage [22]. In the webpage, the starting time (t_0), the polarization of the blue (yellow) beam at the beginning of every fill (P_0), the decay rate ($\frac{dP}{dt}$) are provided for each fill. For each event, the beam polarization can be calculated from the time difference from the beginning of the fill using Equ. (8.1), where t_{event} is the time of each event. The beam polarization for each run can be calculated by Equ. (8.2), where t_{run} is the time of the center of the run. The beam polarization for each fill can be calculated using the weighted average run polarization with Equ. (8.3), where L_{run} is the luminosity of each run. However, since L_{run} is proportional to the number of events in each run, the number of events in each run will be replacing the luminosity of each run in the calculation.

$$P_{event} = P_0 + \frac{dP}{dt}(t_{event} - t_0) \tag{8.1}$$

$$P_{run} = P_0 + \frac{dP}{dt}(t_{run} - t_0) \tag{8.2}$$

$$P_{fill} = \frac{\sum_{run} L_{run} P_{run}}{\sum_{run} L_{run}} \tag{8.3}$$

The beam polarization uncertainty includes the scale uncertainty, fill-to-fill uncertainty, and uncertainty from the profile correction procedure [23].

The scale uncertainty is related to the polarization measurement methods. It includes H-jet scale, H-jet background and pC scale. For run 15, the scale uncertainty is 3% [23].

The relative uncertainty of the profiles correction for one beam in one fill is 2.2%. For a set of M fills, the relative profile correction for the single-spin asymmetry measurement is $\sigma(profile)/P = 2.2\%/\sqrt{M}$ [23]. For the run 15 FMS dataset, this uncertainty is about 0.3%.

The fill-to-fill uncertainty is propagated based on Equ. (8.3) with the uncertainty of P_0 and $\frac{dP}{dt}$. The uncertainty for these two terms ($\sigma(P_0)$) and ($\sigma(\frac{dP}{dt})$) for either blue beam or yellow beam can be obtained in [22]. This uncertainty can be expressed in Equ. (8.4). The third term on the right side of the equation is due to the sensitivity of the measurement of the energy scale of the nuclei in the pC polarimetry [14], and it's negligible. However, for the term (Equ. (8.5)), this correction is overcounting for the measurement using a fraction of the run period. Therefore, a correction scale factor $\sqrt{1-\frac{M}{N}}$ is applied for the second term, which is shown in Equ. (8.6). For this analysis, N=54 and M=142. The fill-to-fill uncertainty for single diffractive EM-jet analysis is about 0.3%.

$$\sigma^2(P_{fill}) = \sigma^2(P_0)+\sigma^2(\frac{dP}{dt})\cdot(\frac{\sum_{run} t_{run}L_{run}}{L_{fill}}-t_0)^2+(\frac{\sigma(fill-to-fill)}{P})^2\cdot P_{fill}^2 \tag{8.4}$$

$$P_{set}^2 = (\frac{\sum_{run} t_{run}L_{run}}{L_{fill}}) \tag{8.5}$$

$$P_{fill-to-fill\ scale}^2 = (1-\frac{N}{M})\cdot P_{set}^2 \tag{8.6}$$

Finally, the polarization uncertainty is calculated in the quadrature. For the single diffractive EM-jet analysis, it's about 3%.

8.6 Summary for the systematic uncertainty

The final systematic uncertainty for single diffractive process and rapidity gap events will be counted bin by bin (x_F bin), and they are calculated as $\sqrt{\sum_i \sigma_i^2}$.

Table (8.3) and Table (8.4) show the systematic uncertainty for each and final term for the blue beam A_N and yellow beam A_N for all photon multiplicity EM-jets from single diffractive process, respectively. Table (8.5) and Table (8.6) show the systematic uncertainty for each and final term for the blue beam A_N and yellow beam A_N for one or two-photon multiplicity EM-jets from single diffractive process, respectively. Table (8.7) and Table (8.8) show the systematic uncertainty for each and final term for the blue beam A_N and yellow beam A_N for three or more photon multiplicity EM-jets from single diffractive process, respectively.

x_F	Small BBC east	Large BBC east	Ring of Fire	Background	Summary
0.2 - 0.25	0.0026	0.0041	0	0.0044	0.0064
0.25 - 0.3	0	0	0.0022	0.0034	0.0041
0.3 – 0.35	0	0.0020	0	0.0032	0.0037
0.35 – 0.4	0.0017	0.0034	0	0.0035	0.0052
0.4 – 0.45	0.0022	0.0052	0.012	0.0041	0.014

Table 8.3: Systematic uncertainty for blue beam A_N for all photon multiplicity EM-jets from single diffractive process

x_F	Small BBC east	Large BBC east	Ring of Fire	Background	Summary
0.2 - 0.25	0.0027	0.0054	0	0.0043	0.0074
0.25 - 0.3	0.0028	0.0025	0	0.0034	0.0051
0.3 – 0.35	0	0.0046	0	0.0031	0.0056
0.35 – 0.4	0.0018	0.0048	0.0051	0.0035	0.0080
0.4 – 0.45	0.0013	0.0022	0	0.0040	0.0048

Table 8.4: Systematic uncertainty for yellow beam A_N for all photon multiplicity EM-jets from single diffractive process

Also, table (8.9) and Table (8.10) show the systematic uncertainty for each and final term for the blue beam A_N and yellow beam A_N for all photon multiplicity EM-jets from rapidity gap events, respectively. Table (8.11) and Table (8.12) show the systematic uncertainty for each and final term for the blue beam A_N and yellow beam A_N for one or two-photon multiplicity EM-jets from rapidity gap events, respectively. Table (8.13) and Table (8.14) show the systematic uncertainty for each and final term for the blue beam A_N and yellow beam A_N for three or more photon multiplicity EM-jets from rapidity gap events, respectively.

Finally, Table (8.15) and Table (8.16) show the systematic uncertainty for each and final term for the blue beam A_N and yellow beam A_N for one or two-photon multiplicity EM-jets from semi-exclusive process, respectively.

x_F	Small BBC east	Large BBC east	Ring of Fire	Background	Summary
0.2 - 0.25	0.0040	0.0033	0	0.0057	0.0077
0.25 - 0.3	0.0024	0	0.0022	0.0046	0.0056
0.3 – 0.35	0.0018	0.0018	0	0.0044	0.0051
0.35 – 0.4	0.0032	0.0034	0	0.0047	0.0066
0.4 – 0.45	0.0055	0.0072	0.022	0.0052	0.024

Table 8.5: Systematic uncertainty for blue beam A_N for 1 or 2 photon multiplicity EM-jets from single diffractive process

x_F	Small BBC east	Large BBC east	Ring of Fire	Background	Summary
0.2 - 0.25	0.0035	0	0	0.0056	0.0065
0.25 - 0.3	0.0021	0.0035	0	0.0045	0.0061
0.3 – 0.35	0.0025	0.0041	0	0.0043	0.0064
0.35 – 0.4	0	0.0062	0	0.0046	0.0077
0.4 – 0.45	0.0016	0.0036	0.020	0.0052	0.021

Table 8.6: Systematic uncertainty for yellow beam A_N for 1 or 2 photon multiplicity EM-jets from single diffractive process

x_F	Small BBC east	Large BBC east	Ring of Fire	Background	Summary
0.2 - 0.25	0	0.0076	0	0.0068	0.010
0.25 - 0.3	0.0022	0.0028	0.0023	0.0051	0.0066
0.3 – 0.35	0	0	0	0.0046	0.0046
0.35 – 0.4	0	0.0047	0.0076	0.0055	0.010
0.4 – 0.45	0.0035	0.0053	0	0.0066	0.0091

Table 8.7: Systematic uncertainty for blue beam A_N for 3 or more photon multiplicity EM-jets from single diffractive process

x_F	Small BBC east	Large BBC east	Ring of Fire	Background	Summary
0.2 - 0.25	0.0098	0.014	0	0.0067	0.019
0.25 - 0.3	0.0037	0.0033	0	0.0046	0.0071
0.3 – 0.35	0.0030	0.0081	0.0046	0.0045	0.011
0.35 – 0.4	0.0037	0.0047	0.0051	0.0052	0.011
0.4 – 0.45	0	0	0.015	0.0065	0.017

Table 8.8: Systematic uncertainty for yellow beam A_N for 3 or more photon multiplicity EM-jets from single diffractive process

x_F	Small BBC east	Large BBC east	Ring of Fire	Summary
0.1 - 0.2	0	0.0064	0	0.0064
0.2 - 0.25	0.0016	0	0	0.0016
0.25 - 0.3	0.00051	0.00096	0.00042	0.0011
0.3 – 0.35	0.00084	0	0	0.00084
0.35 – 0.4	0.0014	0	0.0033	0.0036
0.4 – 0.45	0.0010	0.0011	0	0.0015

Table 8.9: Systematic uncertainty for blue beam A_N for all photon multiplicity EM-jets from rapidity gap events

x_F	Small BBC east	Large BBC east	Ring of Fire	Summary
0.1 - 0.2	0.0027	0	0	0.0027
0.2 - 0.25	0.00052	0.0019	0	0.0019
0.25 - 0.3	0.00064	0.0012	0	0.0013
0.3 – 0.35	0.00066	0.00047	0	0.00081
0.35 – 0.4	0.00092	0.0013	0.0023	0.0029
0.4 – 0.45	0	0.0012	0	0.0012

Table 8.10: Systematic uncertainty for yellow beam A_N for all photon multiplicity EM-jets from rapidity gap events

x_F	Small BBC east	Large BBC east	Ring of Fire	Summary
0.1 - 0.2	0.0028	0.0061	0	0.0067
0.2 - 0.25	0.0018	0.0019	0	0.0026
0.25 - 0.3	0	0	0.00070	0.00070
0.3 – 0.35	0.00094	0	0.0023	0.0025
0.35 – 0.4	0.0024	0.0017	0	0.0030
0.4 – 0.45	0.00074	0.0019	0	0.0020

Table 8.11: Systematic uncertainty for blue beam A_N for 1 or 2 photon multiplicity EM-jets from rapidity gap events

x_F	Small BBC east	Large BBC east	Ring of Fire	Summary
0.1 - 0.2	0.0027	0	0	0.0027
0.2 - 0.25	0.00081	0.0024	0	0.0018
0.25 - 0.3	0.0015	0.0011	0	0.0019
0.3 – 0.35	0.00086	0.0011	0.0017	0.0022
0.35 – 0.4	0	0.0015	0.0034	0.0037
0.4 – 0.45	0.00069	0	0.0059	0.0060

Table 8.12: Systematic uncertainty for yellow beam A_N for 1 or 2 photon multiplicity EM-jets from rapidity gap events

x_F	Small BBC east	Large BBC east	Ring of Fire	Summary
0.1 - 0.2	0	0.0088	0	0.0088
0.2 - 0.25	0.0015	0	0	0.0015
0.25 - 0.3	0	0	0	0
0.3 – 0.35	0.00082	0	0.0018	0.0020
0.35 – 0.4	0	0	0.0040	0.0040
0.4 – 0.45	0.0028	0.0021	0.0036	0.0050

Table 8.13: Systematic uncertainty for blue beam A_N for 3 or more photon multiplicity EM-jets from rapidity gap events

x_F	Small BBC east	Large BBC east	Ring of Fire	Summary
0.1 - 0.2	0.0045	0	0	0.0045
0.2 - 0.25	0	0.0028	0	0.0028
0.25 - 0.3	0.0014	0.0026	0	0.0029
0.3 – 0.35	0.0014	0	0	0.0014
0.35 – 0.4	0.0017	0.0014	0	0.0022
0.4 – 0.45	0.0017	0.0021	0.0046	0.0053

Table 8.14: Systematic uncertainty for yellow beam A_N for 3 or more photon multiplicity EM-jets from rapidity gap events

Blue beam x_F	Small BBC west	Large BBC west	Ring of Fire	Energy sum	Background	Summary
0.2 - 0.25	0	0.033	0	0.028	0.0033	0.043
0.25 - 0.3	0.0081	0.021	0	0	0.0031	0.023
0.3 – 0.35	0.0058	0	0.010	0.011	0.0027	0.017
0.35 – 0.4	0.0072	0.011	0	0.040	0.0011	0.041
0.4 – 0.45	0.012	0.015	0	0	0.0045	0.019

Table 8.15: Systematic uncertainty for blue beam A_N for 1 or 2 photon multiplicity EM-jets from semi-exclusive process

Yellow beam x_F	Small BBC west	Large BBC west	Ring of Fire	Energy sum	Background	Summary
0.2 - 0.25	0.018	0.014	0	0	0.00059	0.023
0.25 - 0.3	0.012	0	0.0045	0.027	0.00068	0.030
0.3 – 0.35	0	0.015	0	0.0012	0.0011	0.019
0.35 – 0.4	0	0.010	0.017	0	0.0042	0.020
0.4 – 0.45	0	0	0	0.011	0.0032	0.012

Table 8.16: Systematic uncertainty for yellow beam A_N for 1 or 2 photon multiplicity EM-jets from semi-exclusive process

Chapter 9

A_N Analysis Method and Results

9.1 A_N Extraction

The cross-ratio method is used to extract the A_N, and the corresponding formulas are shown in Equ. (9.1) and Equ. (9.2). In both equations, raw A_N stands for the raw asymmetry. $N^{\uparrow(\downarrow)}(\phi)$, $N^{\uparrow(\downarrow)}(\phi+\pi)$ are the yields detected at ϕ, $(\phi+\pi)$ for spin up (down) state, where ϕ is the azimuthal angle of the EM-jet in the lab frame. In this analysis, the full 2π azimuthal coverage is split into 16 ranges. P is the average polarization of the proton beam, where the polarization for each event is calculated from Equ. (8.1). A cosine fit $(p_0 \cos(\phi) + p_1)$ is applied to the entire data after all the event selection criteria to extract the A_N from the raw asymmetry in Eq. (9.2), while the constant term p_1 could provide cross-check for possible unidentified asymmetry, but this analysis does not take it into account.

$$rawA_N = \frac{\sqrt{N^{\uparrow}(\phi)N^{\downarrow}(\phi+\pi)} - \sqrt{N^{\downarrow}(\phi)N^{\uparrow}(\phi+\pi)}}{\sqrt{N^{\uparrow}(\phi)N^{\downarrow}(\phi+\pi)} + \sqrt{N^{\downarrow}(\phi)N^{\uparrow}(\phi+\pi)}} \tag{9.1}$$

$$\epsilon = PA_N cos(\phi) \tag{9.2}$$

This method takes advantage of detector azimuthal symmetry and cancels effects due to the non-uniform detector efficiency and the time-dependent luminosity.

Figure 9.1 shows one example for the raw asymmetry extraction with the cosine fit applied. Finally, the quality of the cross-ratio fit for all these processes and the cases of photon multiplicity are mentioned in Appendix C.

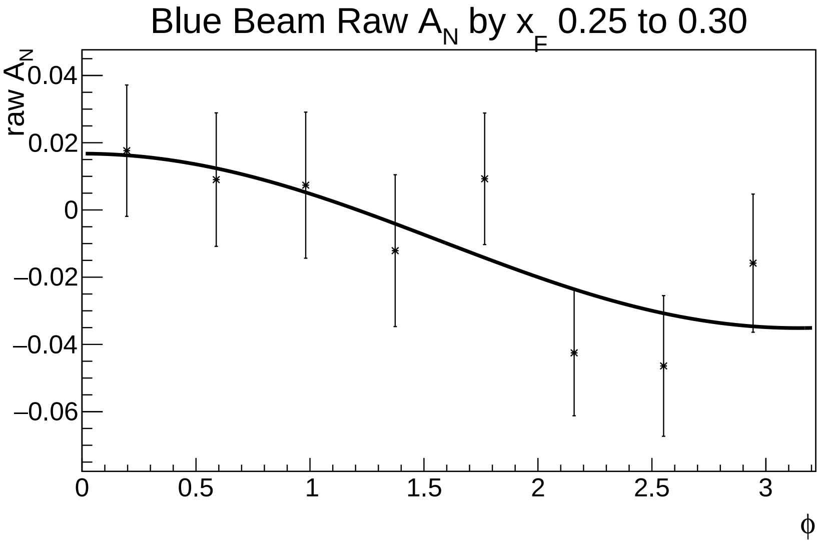

Figure 9.1: Example of the raw asymmetry extraction (raw A_N) with the cosine fit. This is the fit for calculating the raw asymmetry for single diffractive EM-jet A_N with all photon multiplicity at the EM-jet $0.25 < x_F < 0.3$.

9.2 Single diffractive EM-jet A_N

Three cases of EM-jet are studied for A_N of the single diffractive process: the EM-jet with all photon multiplicity, with only one or two-photon multiplicity, and with three or more photon multiplicity. Figure (9.2) shows the results for the single diffractive EM-jet A_N as a function of x_F for the three cases of photon multiplicity mentioned above. Among the three panels in the figure, the blue points are for the blue beam A_N, represented as $x_F > 0$, while the red points are for the yellow beam A_N, represented as $x_F < 0$. The top panel is the results for all photon multiplicity. The statistical uncertainty is shown in bar, while the systematic uncertainty is shown in shaded box. The 2.7 σ non-zero significance is observed for the blue beam A_N. The blue beam A_N for the EM-jets with one or two photon multiplicity case shows about 2.5 σ non-zero significance, showing in the middle panel. However, the blue beam A_N for the EM-jets with three or more photon multiplicity cases is consistent with zero. The EM-jet A_N for one or two-photon multiplicity case is larger than that for all photon multiplicity case and for three or more-photon multiplicity case, which is consistent with the results shown in the inclusive processes [24].

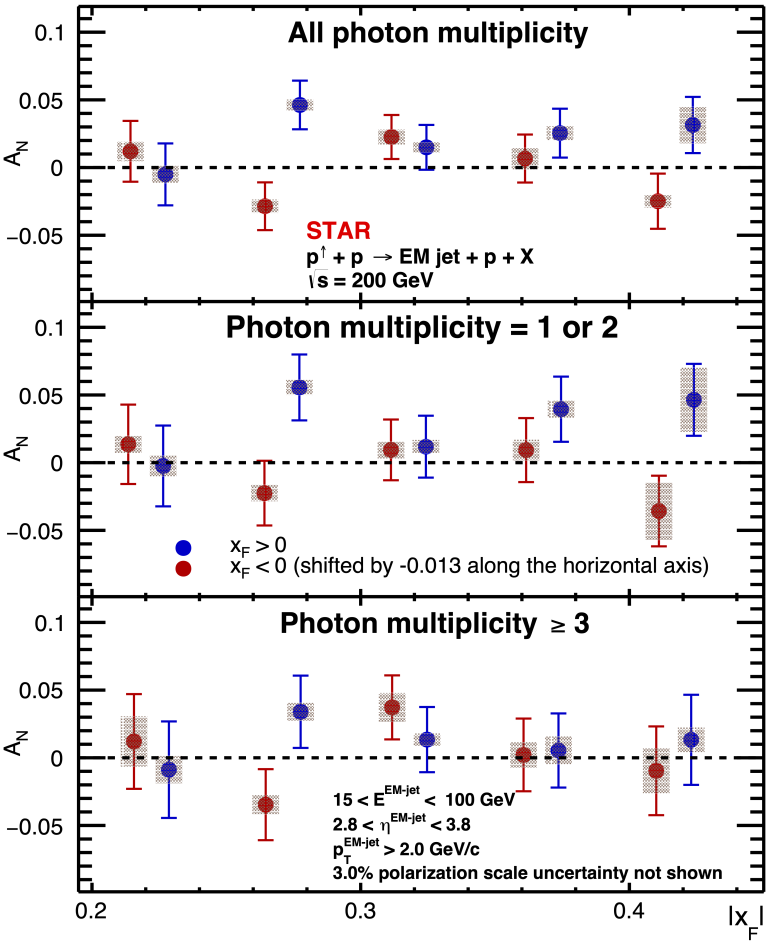

Figure 9.2: A_N for single diffractive events as a function of x_F for three different photon multiplicity cases: all photon multiplicity (top), one or two-photon multiplicity (middle), and three or more photon multiplicity (bottom). The A_N for $x_F < 0$ (red points) shifts -0.013 along the x-axis.

9.3 Rapidity gap events EM-jet A_N

For the A_N of the rapidity gap events, the same three cases of the EM-jet are explored: the EM-jet with all photon multiplicity, with only one or two-photon multiplicity, and with three or more photon multiplicity. Figure (9.3) shows the results for the EM-jet A_N of the rapidity gap events as a function of x_F for the three cases of photon multiplicity mentioned above. The A_N of all photon multiplicity and one or two-photon multiplicity cases shows the non-zero value but with a similar scale as for the A_N of the inclusive process with the same two cases of photon multiplicity [24]. The A_N of the three or more photon multiplicity EM-jets are shown to be consistent with zero. In addition, the yellow beam A_N is also consistent with zero, regardless of photon multiplicity.

Furthermore, to better visualize the A_N contributions of the single diffractive process and the rapidity gap events to the inclusive process, a direct comparison plot among the A_N for inclusive process, diffractive process, and rapidity gap events for one or two-photon multiplicity, and three or more-photon multiplicity are shown in Fig. (9.4). The A_N for the single diffractive process and the rapidity gap events are consistent with that for inclusive process within uncertainty coverage for most of the x_F regions for both multiplicity cases. The A_N for the three processes for EM-jets with three or more-photon multiplicity are all consistent with each other. These direct comparison results indicate that the single diffractive process can not provide evidence that it contributes to the large A_N in the inclusive process.

9.4 Semi-exclusive EM-jet A_N

For the semi-exclusive process, only the case of EM-jet with 1 or 2 photon is explored to extract the A_N, because the majority of the events are with 1 or 2 photon multiplicity EM-jet. Figure (9.5) shows the semi-exclusive EM-jet A_N as a function of EM-jet x_F. Constant fit is applied to check the n-sigma significance for non-zero A_N value among these x_F regions. The blue beam A_N is 3.1σ to be non-zero, while the yellow beam A_N is 1.4σ to be non-zero. However, the semi-exclusive EM-jet A_N is negative, which is different from A_N in the inclusive process. Further theories are needed to understand such different sign.

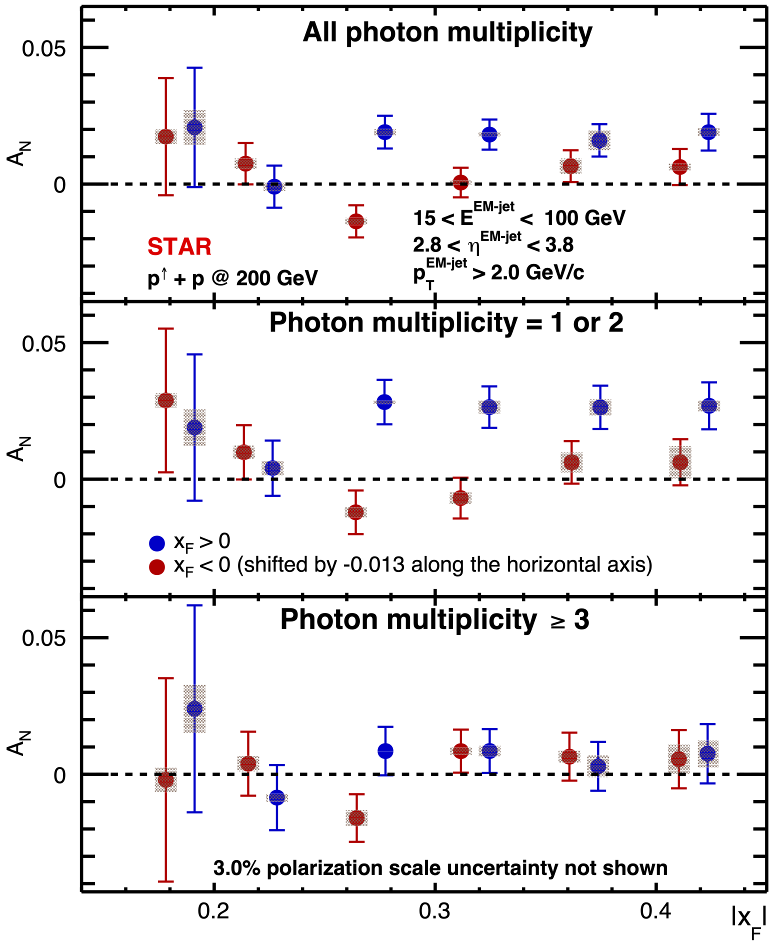

Figure 9.3: A_N for rapidity gap events as a function of x_F for three different photon multiplicity cases: all photon multiplicity (top), one or two-photon multiplicity (middle), and three or more photon multiplicity (bottom). The A_N for $x_F < 0$ (red points) shifts -0.013 along the x-axis.

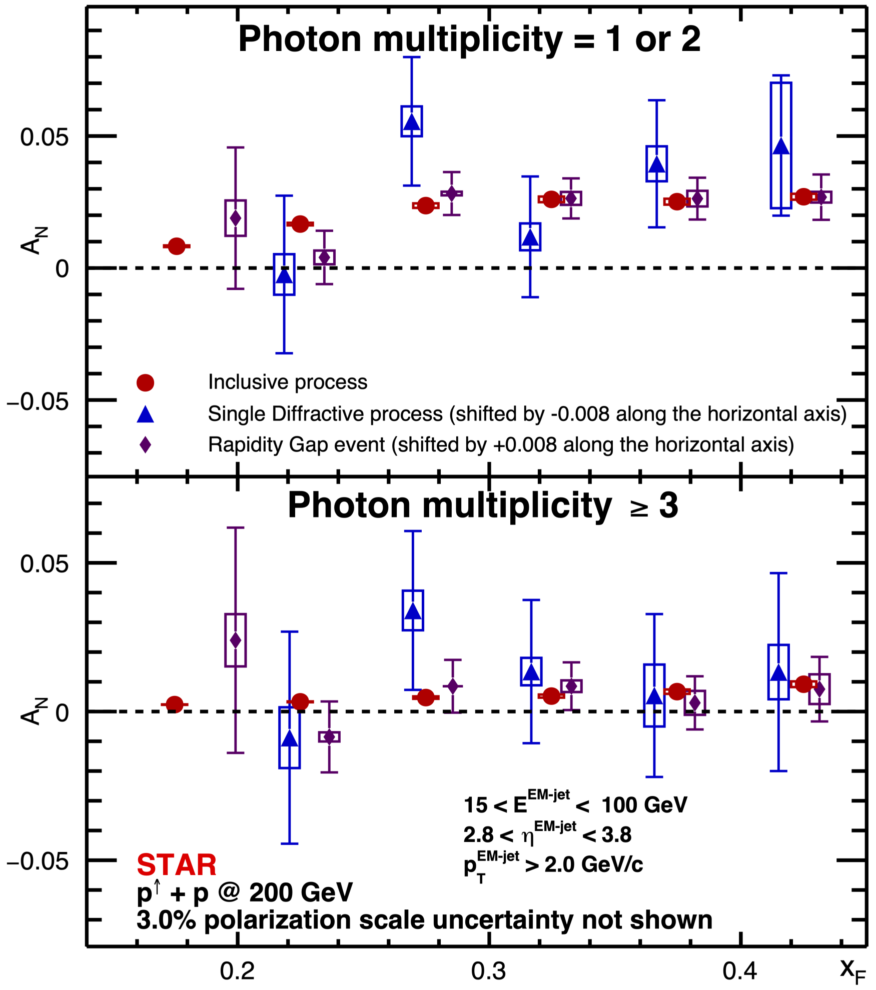

Figure 9.4: A_N for inclusive process (red), single diffractive process (blue), and the rapidity gap events (purple) as a function of x_F for one or two-photon multiplicity case (top panel) and three or more-photon multiplicity (bottom panel). The A_N for single diffractive process shifts -0.008 along the x-axis, and the A_N for rapidity gap events shifts +0.008 along the x-axis

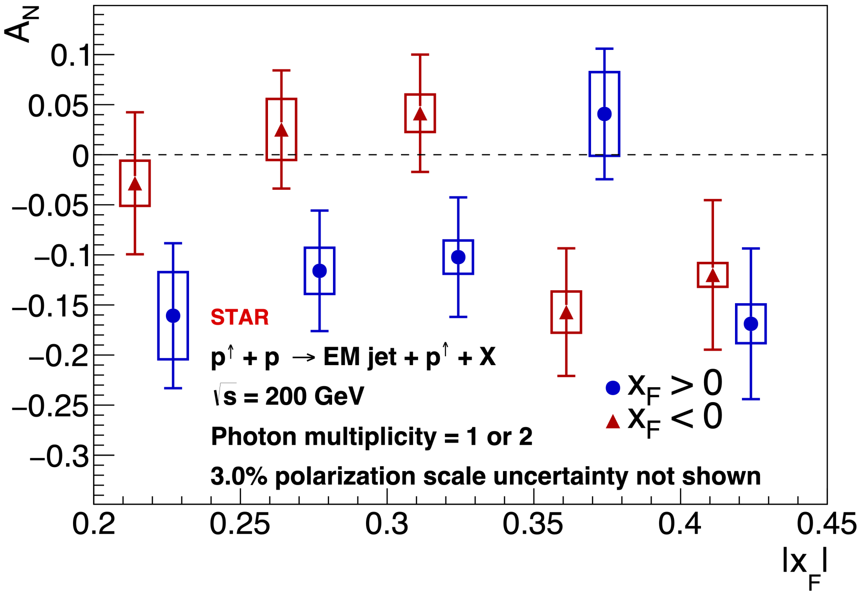

Figure 9.5: A_N for the semi-exclusive process with 1 or 2 photon multiplicity EM-jets as a function of EM-jet x_F. The blue points are for $x_F > 0$, while the red points are for $x_F < 0$.

Chapter 10

Cross section fraction study

The cross section fraction is the fraction of the cross section in the single diffractive process to the cross section in the inclusive process at forward region. This study can provide evidence to develop theories to understand the underlying mechanism for the A_N in the diffractive process.

The cross section for the single diffractive process (σ_{SD}) can be calculated using Equ. (10.1). The cross section for the inclusive process (σ_{inc}) can be calculated using Equ. (10.2). N_{SD} and N_{inc} denote as the yields of single diffractive events and inclusive events, respectively. To specify, the inclusive event yields only counts the runs used for the single diffractive events. ε_{RP} and ε_{BBC} are the Roman Pot efficiency and BBC efficiency, respectively. Purity indicate the fraction of the real single diffractive process in the single diffractive process. ε_{FMS} denotes as FMS efficiency, $\varepsilon_{trigger}$ denotes as trigger efficiency, $\pounds$ denotes as integrated luminosity. However, it is difficult to calculate the FMS efficiency and the trigger efficiency. Therefore, we do not calculate the absolute cross section for either process. However, if we assume the FMS efficiency, the trigger efficiency and the integrated luminosity are the same between two processes, all these terms can cancel out between each other when we calculate their ratio. In that case, the cross section fraction can be calculated using Equ. (10.3).

$$\sigma_{SD} = \frac{N_{SD} \times purity}{\pounds \times \varepsilon_{RP} \times \varepsilon_{BBC} \times \varepsilon_{FMS} \times \varepsilon_{trigger}} \tag{10.1}$$

$$\sigma_{inc} = \frac{N_{inc}}{\pounds \times \varepsilon_{FMS} \times \varepsilon_{trigger}} \tag{10.2}$$

$$\frac{\sigma_{SD}}{\sigma_{inc}} = \frac{N_{SD} \times purity}{N_{inc} \times \varepsilon_{RP} \times \varepsilon_{BBC}} \tag{10.3}$$

Purity can be calculated using the zerobias event background estimation (detail in Sec. (7.1)). The fraction of the accidental coincidence is $1.8\% \pm 0.1\%$, so the purity is $98.2\% \pm 0.1\%$.

The RP efficiency can be estimated using the single diffractive process simulation using the Pythia simulation and RP simulation (pp2pp). It can be calculated by the fraction of the events with good east RP track after the RP simulation in the detector level to the events with proton on east side in the Pythia simulation in the particle level. Both the good east RP track in the RP simulation and the proton track in the particle level simulation are required to be within $0 < \xi < 0.15$ region. The RP efficiency is about 11.4%.

The BBC efficiency be estimated using the single diffractive process simulation using the Pythia simulation and STAR simulation (Geant3) with BBC simulation option. This efficiency can be calculated by the fraction of the events passing the BBC east veto (detail in Sec. (3.3)) to all the events with east proton intact. The BBC efficiency is about 99.9%.

The systematic uncertainty for the RP efficiency is 6.5%, based on the STAR central exclusive analysis [25]. The systematic uncertainty for the BBC efficiency is 10%, based on STAR single diffractive study [26].

The overall cross section fraction is $0.672\% \pm 0.080\%$. The differential cross section is studied as a function of EM-jet x_F region, shown in Fig. (10.1). The single diffractive process cross section is very small compared to the inclusive process cross section, which shows that it can not have significant contribution to the large A_N in inclusive process.

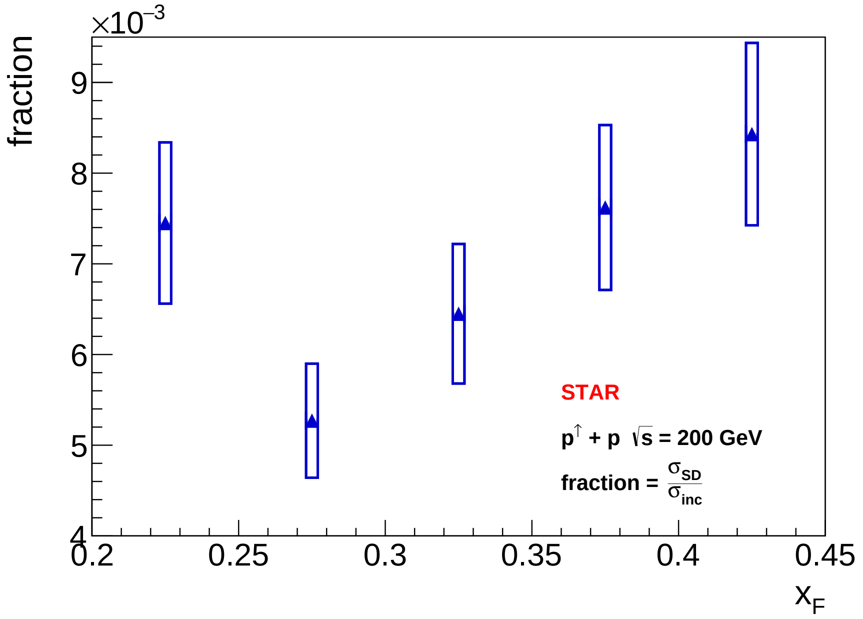

Figure 10.1: Cross section fraction of the single diffractive process (σ_{SD}) to the inclusive process (σ_{inc}) as a function of x_F.

Chapter 11

Conclusion

The transverse single-spin asymmetry as a function of EM-jet x_F from single diffractive process is explored. The all photon multiplicity and one or two-photon multiplicity EM-jet A_N for $x_F > 0$ from the single diffractive process show the non-zero values with more than 2-σ significance. The A_N for $x_F < 0$ from the single diffractive process and rapidity gap events are shown to be consistent with zero. Furthermore, the A_N for inclusive process, the single diffractive process, and the rapidity gap events are consistent with each other within uncertainty. In addition, the cross section fraction study provide evidence that the single diffractive process cross section is very small compared to the inclusive process cross section. Therefore, no strong evidence exists that these process with the unpolarized proton intact will contribute to the large A_N in the inclusive process.

The transverse single-spin asymmetry for semi-exclusive process with polarized proton intact is negative with more than 3σ significance to be non-zero, which also can not have great contribution to the large A_N in the inclusive process. Such a different sign on the A_N requires further theories to explain.

Appendix A

Run list

Table A.1: Run list

16066033	16066035	16066046	16066047	16066049	16066050	16066051
16066052	16066053	16066054	16066055	16066059	16066060	16067001
16067003	16067004	16067005	16067006	16067013	16067014	16067015
16067016	16067017	16067019	16067020	16067021	16067022	16068022
16068023	16068024	16068025	16068028	16068029	16068030	16068032
16068034	16068035	16068036	16068037	16068038	16068039	16068040
16068042	16068055	16068056	16068057	16068058	16069001	16069002
16069003	16069004	16069005	16069006	16069007	16069008	16069009
16069010	16069011	16069012	16069016	16069053	16069054	16069055
16069060	16069062	16069063	16069064	16069065	16069066	16069067
16070003	16070004	16070005	16070006	16070008	16070009	16070010
16070012	16070013	16070014	16070015	16070039	16071001	16071002
16071003	16071006	16071007	16071010	16071016	16071018	16071021
16071022	16071023	16071024	16071025	16071026	16071027	16071043
16071044	16071045	16071046	16071050	16071051	16071052	16071053
16071054	16071055	16071056	16071058	16071059	16071060	16071061
16071062	16071076	16071077	16071078	16071079	16072001	16072002
16072003	16072006	16072007	16072008	16072009	16072010	16072012
16072013	16072014	16072021	16072022	16072023	16072024	16072025

Continued on next page

Table A.1: Run list (Continued)

16072026	16072033	16072034	16072035	16072036	16072038	16072039
16072040	16072041	16072042	16072043	16072046	16072047	16072057
16072058	16072059	16072060	16072061	16072062	16073001	16073017
16073018	16073019	16073020	16073021	16073030	16073031	16073032
16073033	16073034	16073035	16073037	16073038	16073039	16073040
16077021	16077027	16077028	16077029	16077030	16077031	16077032
16077033	16077034	16077037	16077038	16077039	16077040	16077041
16077043	16077044	16077045	16077046	16077047	16077054	16077055
16078001	16078002	16078003	16078004	16078005	16078006	16078007
16078008	16078009	16078011	16078012	16078013	16078014	16078028
16078029	16078030	16078031	16078032	16078033	16078034	16078035
16078036	16078037	16078038	16078039	16078040	16078041	16078042
16078055	16078056	16079001	16079010	16079011	16079013	16079014
16079015	16079016	16079017	16079018	16079019	16079020	16079021
16079022	16079023	16079024	16079027	16079028	16079029	16079030
16079031	16079032	16079033	16079034	16079035	16079036	16079045
16079046	16079047	16079054	16079057	16079058	16079059	16079060
16079061	16079062	16079063	16080002	16080003	16080004	16080005
16080006	16080007	16080012	16080013	16080014	16080015	16080020
16080021	16080022	16080023	16080024	16080025	16080026	16080027
16080028	16080029	16080030	16080031	16080032	16080033	16080043
16080044	16080045	16080046	16080047	16080048	16080049	16080050
16080051	16080052	16080053	16080054	16080055	16081001	16081002
16081003	16081004	16081012	16081013	16081015	16081016	16081017
16081018	16081019	16081020	16081021	16081022	16081024	16081025
16081036	16081037	16081048	16081049	16081050	16081052	16081053
16081054	16081055	16081056	16081057	16081058	16081059	16081060
16081061	16082001	16082002	16082011	16082012	16082013	16082017
16082018	16082019	16082022	16082023	16082025	16082027	16082028

Continued on next page

Table A.1: Run list (Continued)

16082029	16082039	16082040	16082041	16082042	16082043	16082045
16082046	16082047	16082048	16082049	16082050	16082051	16082052
16082053	16082054	16082055	16082056	16082057	16083004	16083005
16083006	16083007	16083008	16083009	16083010	16083011	16083012
16083013	16083014	16083015	16083016	16083017	16083018	16083019
16083041	16083042	16083043	16083044	16083045	16083046	16083048
16083049	16083050	16083052	16083053	16083055	16083056	16083057
16083058	16083059	16083060	16084004	16084006	16084007	16084008
16084009	16084011	16084012	16084013	16084014	16084015	16085005
16085006	16085007	16085008	16085009	16085011	16085012	16085013
16085014	16085023	16085024	16085025	16085026	16085027	16085028
16085029	16085030	16085031	16085032	16085033	16085035	16085036
16085037	16085051	16085052	16085054	16085055	16085056	16085057
16085058	16085061	16085062	16085065	16085067	16085069	16085071
16085072	16085073	16085074	16086001	16086002	16086003	16086004
16086005	16086006	16086007	16086008	16086024	16086025	16086026
16086027	16086028	16086030	16086031	16086032	16086033	16086034
16086035	16086036	16086037	16086038	16086039	16086040	16086041
16086042	16086050	16086051	16086052	16086053	16086054	16087001
16087002	16087003	16087004	16087005	16087006	16087007	16087008
16087009	16087010	16087011	16087019	16087020	16087021	16087022
16087023	16087024	16087025	16087026	16087027	16087028	16087029
16087030	16087031	16087032	16087033	16087041	16087042	16087043
16087044	16087045	16087046	16087047	16087048	16087049	16087050
16087051	16087052	16087053	16087054	16087055	16088001	16088013
16088016	16088017	16088018	16088019	16088020	16088021	16088022
16088023	16088025	16088026	16088027	16088028	16088029	16088030
16088031	16088040	16088041	16088042	16088043	16088044	16088045
16088046	16088047	16088048	16088049	16088050	16089001	16089002

Continued on next page

Table A.1: Run list (Continued)

16089003	16089004	16089005	16089015	16089016	16089017	16089018
16089019	16089020	16089024	16089026	16089027	16089028	16089029
16089030	16089031	16089041	16089042	16089043	16089044	16089045
16089046	16089047	16089048	16089049	16089050	16089051	16089052
16089053	16089054	16090001	16090002	16090003	16090004	16090005
16090015	16090016	16090017	16090018	16090019	16090020	16090021
16090022	16090023	16090024	16090025	16090026	16090027	16090028
16090029	16090030	16090038	16090039	16090041	16090042	16090044
16090045	16090046	16090047	16090048	16090049	16090050	16090051
16090052	16090053	16091003	16091004	16091005	16091006	16091007
16091008	16091009	16091010	16091011	16091012	16091013	16091014
16091039	16091040	16091042	16091057	16091061	16091062	16091063
16092001	16092002	16092003	16092014	16092015	16092016	16092017
16092018	16092019	16092020	16092021	16092022	16092023	16092031
16092033	16092034	16092035	16092036	16092037	16092040	16092042
16092044	16092048	16092049	16092050	16092051	16092052	16092053
16092054	16092055	16092063	16092064	16092065	16092066	16092067
16092068	16092069	16092070	16092071	16093001	16093002	16093003
16093004	16093010	16093011	16093012	16093013	16093014	16093015
16093016	16093017	16093018				

Appendix B

Derivation for the AC events effect to the uncertainty

The effect for the uncertainty in A_N calculation regarding the AC events is derived as follows. First of all, the corrected A_N is shown in Equ. (B.1). $A_N(sig)$ is the corrected A_N, while $A_N(mea)$ is the measured A_N which contains the effect of AC events. $frac(sig)$ is the signal fraction, while $frac(bkg)$ is the AC background fraction, which is about 1.8% (detailed in Sec. (7.1)). The error propagation for Equ. (B.1) is expressed in Equ. (B.2). Since the AC background fraction and its uncertainty are very small, the second and the third term are neglectable. Therefore, only the first term related to the statistical uncertainty of the measured asymmetry will be kept. The difference in the uncertainty between with and without the AC event correction will be assigned as systematic uncertainty.

$$A_N(sig) = \frac{A_N(mea) - frac(bkg) * A_N(bkg)}{frac(sig)} = \frac{A_N(mea) - frac(bkg) * A_N(bkg)}{1 - frac(bkg)} \tag{B.1}$$

$$
\begin{aligned}
\sigma^2 &= (\frac{\partial A_N(sig)}{\partial A_N(mea)})^2 \sigma A_N^2(mea) + (\frac{\partial A_N(sig)}{\partial frac(bkg)})^2 \sigma frac^2(bkg) + (\frac{\partial A_N(sig)}{\partial A_N(bkg)})^2 \sigma A_N^2(bkg) \\
&= (\frac{1}{1-frac(bkg)})^2 \sigma A_N^2(mea) + (\frac{A_N(sig)}{1-frac(bkg)})^2 \sigma frac^2(bkg) + (\frac{frac(bkg)}{1-frac(bkg)})^2 \sigma A_N^2(bkg) \\
&= (\frac{1}{frac(sig)})^2 \sigma A_N^2(mea) + (\frac{A_N(sig)}{frac(sig)})^2 \sigma frac^2(bkg) + (\frac{frac(bkg)}{frac(sig)})^2 \sigma A_N^2(bkg) \\
&\approx (\frac{1}{frac(sig)})^2 \sigma A_N^2(mea)
\end{aligned}
\tag{B.2}
$$

Appendix C

Cross-ratio fit quality results

Figure C.1 shows the χ^2 for the fit on extracting the A_N for all the three processes mentioned in this note. The χ^2 probability distribution with degree of freedom equal to 6)this analysis) is also shown in Fig. (C.2. They are roughly matched. Figure C.3 shows the distribution of the constant term from the fit divided by its uncertainty. A Gaussian fit is applied to check whether the constant term is consistent with zero. The mean of the Gaussian fit is -0.15 ± 0.16 and the width is 1.1 ± 0.15, which show that the constant term is consistent with zero within uncertainty.

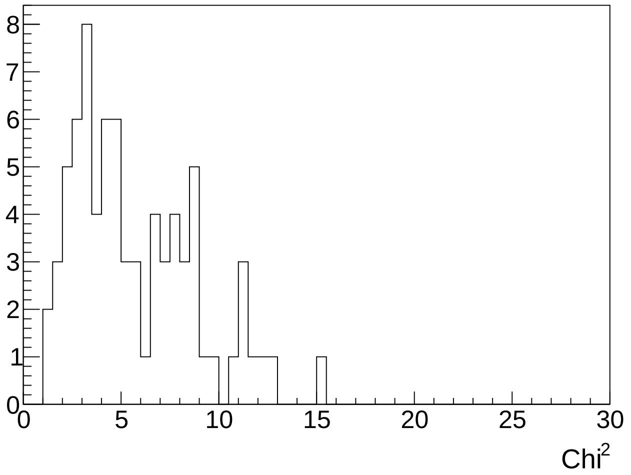

Figure C.1: χ^2 for the fit for all the data points for all three processes.

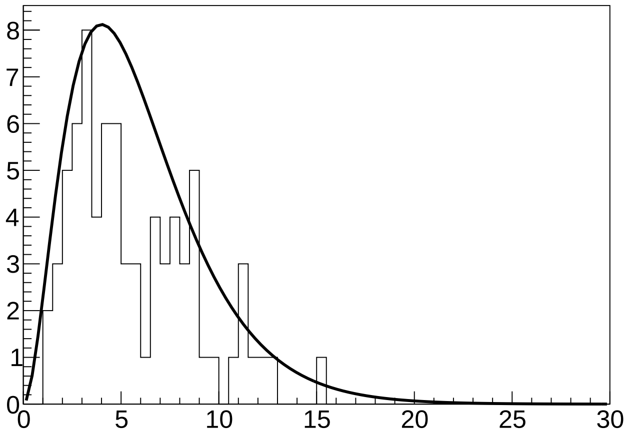

Figure C.2: χ^2 for the fit for all the data points for all three processes (in histogram). The curve shows the χ^2 probability distribution with degree of freedom = 6.

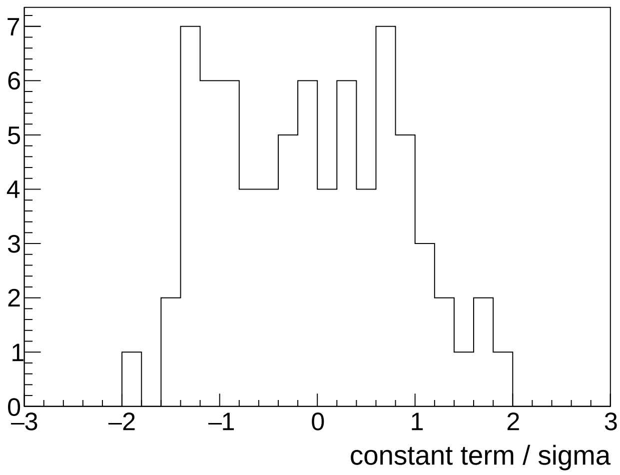

Figure C.3: Distribution of the constant term from the fit divided by its uncertainty

Bibliography

[1] D.L. Adams *et al.*, Phys. Lett. B 261, 201(1991)

[2] B.I. Abelev *et al.* (STAR Collaboration), Phys. Rev. Lett. 101, 222001(2008)

[3] A. Adare *et al.* Phys. Rev. D 90, 012006 (2014)

[4] E.C. Aschenauer *et al.*, arXiv:1602.03922

[5] J. Adam *et al.* (STAR Collaboration), Phys. Rev. D 103, 092009 (2021)

[6] G. L. Kane, J. Pumplin, and W. Repko. Phys. Rev. Lett. 41, 1689 (1978)

[7] D. Sivers, Phys. Rev. D 41, 83 (1990)

[8] J. Collins, Nucl Phys B 396 (1993) 161

[9] J.W. Qiu and G. Sterman, Phys. Rev. Lett. 67 2264 (1991)

[10] V. Khachatryan *et al.* (CMS Collaboration)

[11] M.M. Mondal (STAR Collaboration) PoS (DIS2014) 216 Phys. Rev. D 92, 012003 (2015)

[12] C. Kim, https://drupal.star.bnl.gov/STAR/starnotes/private/psn0735

[13] M.Cacciari, G. P. Salam, and G. Soyez, Eur. Phys. J. C (2012) 72: 1896

[14] Z. Zhu, https://drupal.star.bnl.gov/STAR/system/files/AnalysisNote_0601_0.pdf

[15] J. Adam *et al.* (STAR Collaboration), Results on Total and Elastic Cross Sections in Proton–Proton Collisions at $\sqrt{s} = 200$ GeV, Phys. Lett. B 808 (2020) 135663

[16] Particle Data Group, The review of particle physics, Prog. Theor. Exp. Phys. (2020) 083C01.

[17] B. B. Abelev *et al.* (ALICE Collaboration), Phys. Rev. D 91, 112012 (2015)

[18] T. Sjostrand, S. Mrenna, and P. Z. Skands, JHEP 05, 026 (2006)

[19] P. Skands, arXiv:1005.3457

[20] Peter Z. Skands Phys. Rev. D 82, 074018

[21] R. Barlow, Systematic Errors: facts and fictions, arXiv:hep-ex/0207026

[22] Run 15 polarization , https://wiki.bnl.gov/rhicspin/Run_15_polarization

[23] W. B. Schmidke, RHIC polarization for Runs 9-17 , Technical Report BNL-209057-2018- TECH, Brookhaven National Laboratory (2018)

[24] X. Liang (STAR Collaboration) 10.5281/zenodo.7236716

[25] The STAR collaboration., Adam, J., Adamczyk, L. et al. Measurement of the central exclusive production of charged particle pairs in proton-proton collisions at $\sqrt{s} = 200$ GeV with the STAR detector at RHIC. J. High Energ. Phys. 2020, 178 (2020). https://doi.org/10.1007/JHEP07(2020)178

[26] STAR analysis note, Measurement of charged-particle production in single diffractive proton-proton collisions at $\sqrt{s} = 200$ GeV with the STAR detector at RHIC , https://drupal.star.bnl.gov/STAR/system/files/nota.pdf